# 3

# The simulation of deep-sea sediments

## 3.1 Introduction

Deep-sea sediments play a critical role in global biogeochemical cycles. Particulate material delivered to, or formed at the ocean surface and which is not removed whilst settling through the water column will eventually reach the ocean floor, forming a surficial 'fluff' layer at the ocean-sediment interface. Much of this material undergoes diagenetic alteration as it is gradually incorporated deeper into the sediments. Such post-depositional changes involve a multitude of interacting physical (diffusion, advection), biological (bioturbation, metabolism) and chemical (dissolution, oxidation, reduction) processes, often characterized by rapid rate constants and operating on a fine spatial scale. By nature of the extremely remote and hostile location of the benthic environment, many of these processes are poorly characterized. Modelling the diagenetic alteration of material within deep-sea sediments is therefore no easy task and can be numerically expensive. Global carbon cycle models have therefore often simply returned all settling material reaching the ocean floor instantaneously back to the ocean (in dissolved form). However, there are a number of compelling reasons for the explicit representation of the deep-sea sediment system, particularly for application to glacial-interglacial change;

- Dissolved chemical species formed through diagenetic alteration processes may escape the sediments by diffusing out across the sediment-water interface into the ocean. Solid material not transformed in this way will be eventually buried. This burial represents a 'sink' for the chemical constituents of that material. For the system as a whole to be at steady state, such sinks must be balanced by inputs to the ocean-atmosphere, such as via continental weathering or volcanic out-gassing. A simplified system where there are no sources or sinks of a species is considered to be 'closed' with respect to this species. The dynamical response of a closed system is found to be very different from that of an open one where there is a continual throughput [*Hotinski et al.*, 2000; *Kump*, 1993; *Sigman et al.*, 1998]. Particularly where the species in question are potentially limiting nutrients, carbon, or alkalinity, a closed system may not capture the long-term dynamics of the global carbon cycle, and will thus not be capable of correctly accounting for the observed glacial-interglacial variability in atmospheric $CO_2$.
- The explicit consideration of the diagenetic alteration of material delivered to the deep-sea floor allows for realistic estimation of the fractionation preservation of this material in the sediments, and therefore of surface sediment composition. Comparisons between model and observed distributions of major solid constituents ($CaCO_3$, opal, detrital material) provides a powerful diagnostic for optimizing or validating components of the overall system model.
- Finally, representation of deep-sea sediments enables an extensive synthetic sedimentary record to be built up over the course of the model simulation. Perturbations to the system will be recorded as down-core variations in sediment solid and/or isotopic properties. Contrasting artificial sediment tracer signals with those derived from actual cores recovered from the ocean floor provides additional constraints for elucidating the mechanisms involved in glacial-interglacial change [*Berger et al.*, 1996].

Deep-sea sediments and their biogeochemical interaction with the ocean are therefore included as a key component within SUE. However, although sediments in the model are considered at all depths (including the pelagic zone) the schemes used for ocean-sediment interaction are strictly applicable only to the benthic environment. As such, there is no explicit consideration of shelf sedimentary processes. The diagenetic alteration of $CaCO_3$ (separately as both calcite and aragonite) and opal are all represented, with the first order effects of bioturbation and sediment compaction accounted for. However, there is no similar mechanistic representation of processes relating to the diagenetic alteration of particulate (or dissolved) organic matter or detrital particles.

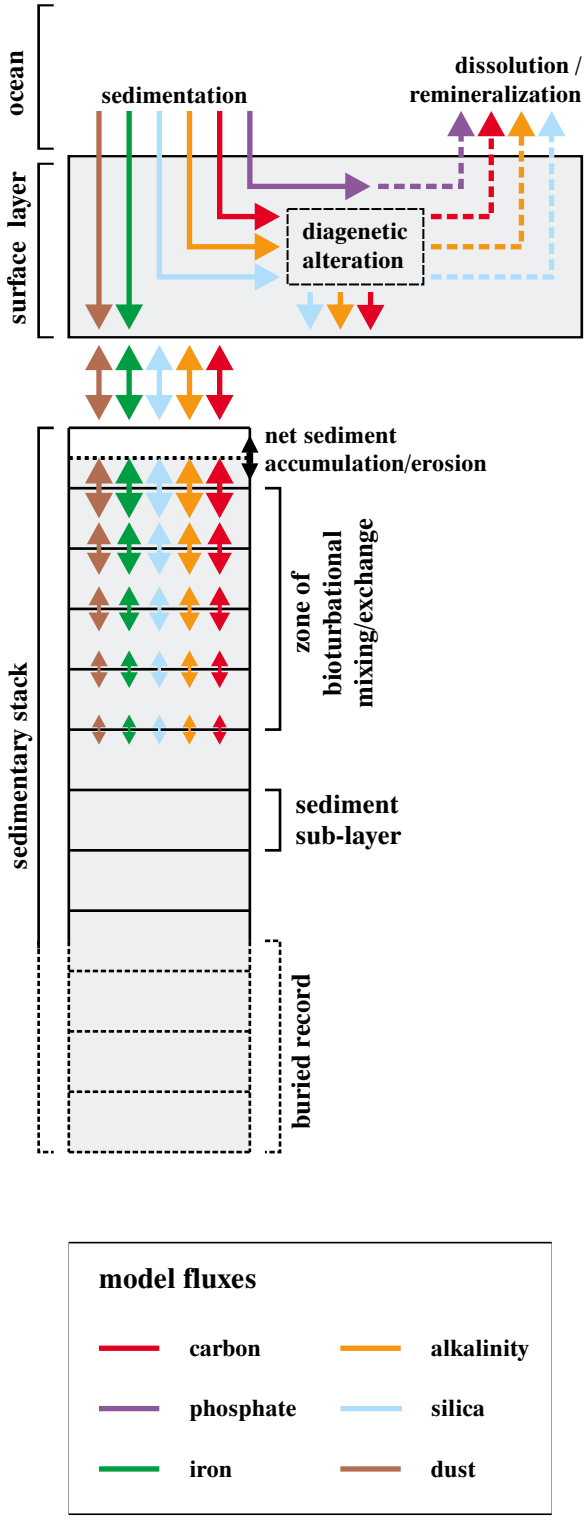


**Figure 3-1** Schematic representation of the sedimentary module within SUE.

## 3.2 Modelling deep-sea sediments

The deep-sea sediment module used in SUE is shown schematically in Figure 3-1. The system comprises a single surface layer underlain by a series of sub-layers. The surface layer represents the upper zone of the sediment where bioturbation effectively homogenizes solid composition with respect to depth, and where the most important diagenetic processes of interest to this present study take place. Solid material which is preserved and exported out of this surface layer (i.e., 'buried') is stored in sedimentary sub-layers lying immediately below. These sub-layers are prescribed a thickness of 1 cm, representing a trade-off between simulated down-core sediment resolution and computational running and storage costs. In addition to the advective transfer of solids between the surface layer and upper-most sediment stack sub-layer (arising from net sedimentary accumulation/erosion) a diffusive-like transfer is prescribed between adjacent sediment layers. This represents the vertical mixing of solids due to biological activity.

Sediment composition within the surface layer is calculated via a simple mass balance and operated asynchronously with the ocean-atmosphere module, such that at time $t = t + 1$

$$M^S_{(t+1)} = M^S_{(t)} + \Delta M^S_{(t)} + Fbal^S \qquad (3\text{-}1)$$

where $M^S_{(t)}$ is the mass of solid component $S$ in the surface layer, and $\Delta M^S_{(t)}$ is the change in mass of this component calculated as the net flux across the sediment-ocean interface

$$\Delta M^S_{(t)} = Fsed^S_{(t)} - Fdis^S_{(t)} \qquad (3\text{-}2)$$

where $Fsed^S_{(t)}$ is the sedimentation (or settling) flux of solid material at the ocean-sediment interface, and $Fdis^S_{(t)}$ is the flux to the ocean of dissolved species derived from the diagenetic alteration of $S$ within the surface layer. $Fbal^S$ is a balancing flux, calculated according to the criterion that there must be no net change in the thickness of the surface layer. Where a net flux across the sediment-water interface results in a volume surfeit of material in the surface layer, a correction is made by removing material from the surface layer and transferring it to the top sub-layer of the sediment stack. Conversely, where the net flux results is a volume deficit, material is removed from the top of the sediment stack and added to the surface layer. This is formally written

$$Fbal^S = -\frac{\sum_S \Delta V^S_{(t)}}{\sum_S V^S_{(t)}} \cdot \left( M^S_{(t)} + \Delta M^S_{(t)} \right) \qquad \sum_S \Delta V^S_{(t)} > 0 \qquad (3\text{-}3a)$$

$$Fbal^S = +\frac{\sum_S \Delta V^S_{(t)}}{\sum_S V^S_{(t)}} \cdot M'^S_{(t)} \cdot \frac{\sum_S V^S_{(t)}}{\sum_S V'^S_{(t)}} \qquad \sum_S \Delta V^S_{(t)} < 0 \qquad (3\text{-}3b)$$

where $M'^S_{(t)}$ is the mass of component $S$ in the uppermost sediment stack sub-layer. Equivalent volumes ($V$) for the mass of each component are defined

$$V^S = \frac{M^S}{\rho^S \cdot \phi} \tag{3-4}$$

where $\rho^S$ is the density of (solid) component *S*, and $\phi$ is the sediment porosity. This transferal procedure is more complicated in practice than this description suggests, since the uppermost sub-layer in the sediment stack has a finite capacity. The situation therefore arises that the effective volume of material to be added to this sub-layer is greater than its remaining (un-filled) capacity. In this case, the incomplete sub-layer is filled first, after which a new sub-layer is created immediately above, which accepts the remaining material. Conversely, when there is a surface deficit, the effective volume of material required may be greater than that remaining within the uppermost sub-layer. All the material in this sub-layer is therefore removed first and the sub-layer destroyed. The residual deficit is then made up by removing material from the new uppermost sub-layer. A simple alternative to this 'open-topped' stack arrangement would be that of an 'open-bottomed' stack [*Heinze et al.*, 1999]. In this scenario all the sub-layers are always complete, with excess material permanently lost or gained from the base. However, this is not only more computationally demanding to implement but is numerically diffusive.

Solid components represented in the sediments include calcite, aragonite, and opal, who all share a biogenic origin in the surface ocean and whose fractional preservation in the sediments is represented explicitly (3.2.4 and 3.2.5). Detrital matter derived from aeolian deposition at the ocean surface is also represented, although it is assumed to act conservatively within the sediments, and no release either $H_4SiO_4$ (from silicates) or dissolved Fe (from Fe-bearing ore and silicate minerals) is considered. Finally, in order to allow glacial-interglacial variability in the isotopic composition of particulate organic carbon to be recorded, POM is simply added to the sediment in a fixed ratio with the flux of material reaching the sediment surface, acting conservatively thereafter. A mean fractional preservation of the POM settling flux of 5% is chosen, consistent with estimates of ~3-7% in deep-sea sediments [*Archer et al.*, submitted; *Tromp et al.*, 1995]. Since the system is not open with respect to $PO_4$, the carbon and phosphorous components of buried POM (together with associated alkalinity) are artificially returned in dissolved form to the overlying surface ocean.

In addition to the representation of solid sedimentary components, a number of isotopic and 'colour' tracers (both conservative and non-conservative) are considered in the sediment module. An isotopic composition for calcite and aragonite is considered, with $^{13}C$ added and removed in proportion to changes in the solid fraction. This proportionality takes a ratio whose value is determined by fractionation processes associated with formation in the ocean surface (2-61a and 2-61b) upon initial deposition to the sediments. Removal from the surface through dissolution or transfer between layers proceeds simply according to a ratio equal to the mean bulk isotopic composition in the layer(s) where the material resides. $^{14}C$ is treated in a similar manner, with the exception that it is decayed with a half life of 5.73 ka. $^{13}C$ in POC is treated in a similar manner to $^{13}C$ in $CaCO_3$. 'Colour' (artificial numerical) tracers are also considered, and used to represent properties such as the age of solid calcite, foraminiferal $\delta^{13}C$ (with planktonic and benthic isotopic signatures considered separately), and foraminiferal $\delta^{18}O$ (again resolved into planktonic and benthic species). These are tied to a solid fraction and treated in a similar manner to that for bulk $^{13}C$, with the exception that the depositional value of benthic and planktonic foraminiferal $\delta^{13}C$ follow (2-62) and (2-63), while benthic and planktonic foraminiferal $\delta^{18}O$ take an isotopic value equal to mean oceanic $\delta^{18}O$, itself prescribed according to the SPECMAP stack [*Imbrie et al.*, 1984]. A final colour tracer is used to represent ash depositional events (3.2.1.2).

At the start of a model run, all sediment modules are initialized with the surface layer and 100 sub-layers entirely composed of detrital material. Steady state is typically reached throughout the ocean with respect to the solid composition in surface sediments on an order of 100 ka.

### 3.2.1 Bioturbation

The vertical (and horizontal) mixing of solid material in the surface zone of deep-sea sediments by the action of benthic organisms (termed 'bioturbation') plays an important role in the dynamical behaviour of the global carbon cycle. For instance, perturbations in ocean chemistry or biological export may lead to the erosion of surface $CaCO_3$. Previously buried material can then be exhumed from depth through bioturbational mixing, thus effectively replenishing the material in the sediment surface [*Archer et al.*, 1998; *Boudreau*, 1994]. If the perturbation continues for an expended period a significant mass of material may eventually be brought to the surface and eroded in this way, thus affecting global ocean chemistry [*Archer et al.*, 1998]. Bioturbation also has important consequences for the interpretation of paleoceanographic proxies [*DuBois and Prell*, 1988; *Ruddiman et al.*, 1980; *Schiffelbein*, 1984; *Trauth*, 1998]. Down-core tracer profiles (such as foraminiferal calcite $\delta^{13}C$ or $\delta^{18}O$) associated with a perturbation event can be 'smeared out' by vertical mixing. This degrades the resolution of the phase information which can be obtained from recovered cores, complicating the analysis of causal links between different processes operating within the system [*Boudreau*, 1994; *Hutson*, 1980]. The apparent magnitude of a perturbation event can also be significantly diminished. Implementation of an adequate sedimentary bioturbation scheme is therefore desirable both for realism in model-generated sediment cores and in capturing system dynamics.

#### *3.2.1.1 Bioturbation model description*

The mechanistic action of benthic organisms leads to the movement of solid material within the surface zone of the sediment. This transfer can occur in both horizontal and vertical planes, may be highly selective in terms of size fraction or chemical composition, and take place throughout a large range of spatial and temporal scales, from an almost

continuous local transport to highly episodic occurrences over an extended distance. The nature of individual disturbances will depend on the animal species involved through behavioural characteristics such as mode of feeding, locomotion, and shelter [*Soetaert et al.*, 1996; *Wheatcroft et al.*, 1990; *Wheatcroft*, 1992]. The abiotic benthic environment also has an important influence, particularly in terms of food source availability [*Legeleux et al.*, 1994; *Trauth et al.*, 1997]. Various detailed mechanistic treatments of bioturbation have been proposed [*Soetaert et al.*, 1996; *Wheatcroft et al.*, 1990; *Trauth*, 1998]. However, such schemes are computationally expensive and require knowledge of benthic ecology which cannot be prognostically provided by SUE. A highly simplified representation of bioturbational mixing in deep sea sediments is therefore required.

The simplest possible treatment is to assume the presence of a relatively thick surface layer, homogeneous in composition over its entire depth [*Berger and Heath*, 1968; *Munhoven and Francois*, 1996]. Such schemes typically assume a thickness of 10 cm for this layer, representing the approximate depth to which deep-sea sediments are often observed to be predominantly 'well-mixed' [*Boudreau*, 1994; *Ikehara et al.*, 2000; *McManus et al.*, 1995]. However, vertical resolution can be improved by assuming that the effect of bioturbation can be modelled as an quasi-diffusive process [*Pope et al.*, 1996; *Wheatcroft et al.*, 1990] and therefore ignoring the effects of non-local mixing [*Boudreau*, 1994; *Legeleux et al.*, 1994; *Soetaert et al.*, 1996; *Wheatcroft*, 1992]. In this, the surface sediment zone is discretized into a series of sub-layers with mixing between adjacent layers characterized by a prescribed biodiffusion coefficient [*Archer*, 1991; *Guinasso et al.*, 1975; *Officer and Lynch*, 1983; *Walker and Opdyke*, 1995].

A variety of simple bioturbational schemes are evaluated here for application in SUE. Potential parameterizations are constrained by the configuration of the sediment module (Figure 3-1) to comprise a homogeneous surface layer overlying a sequence of 1 cm thick stacked layers. The mixing rate between pairs of sub-layers is determined by a biodiffusion coefficient which decreases with depth determined by a profile which can be varied in both shape and magnitude. In the following sections the results from just two of these schemes are presented. The first (designated "10 cm only") is the simplest, consisting of just a 10 cm thick surface layer with no deeper mixing. The second ("5 cm plus deep mixing") is adapted from *Peng et al.* [1979], and comprises a 5 cm thick surface layer with deeper mixing below this. This deep mixing follows an exponentially-decreasing profile of *e*-folding length 1 cm, with a maximum mixing rate (at the base of the surface layer) of 16 $cm^2$ $ka^{-1}$.

**Table 3-1 Ash and Pumice Tracer Sediment Core Details**

| Core | Tracer | Sediment accumulation rate (cm $ka^{-1}$) |
|---|---|---|
| V19-28 | Ash | 7.00 |
| V19-29 | Ash | 7.00 |
| V29-39 | Ash | 0.50 |
| V29-40 | Ash | 0.50 |
| RC17-126 | Ash | 2.00 |
| E48-23 | Pumice | 2.50 |

### *3.2.1.2 Inert tracer profile simulation*

Sub-aerial volcanic events tend to produce airborne ejecta such as ash and pumice in discrete rather transitory pulses. Since the time scale for its deposition to the deep-sea floor is short compared to the residence time of material in the bioturbated zone, the input to the sediments of ash and pumice can be assumed to be effectively instantaneous. An additional advantage of such material as a bioturbation tracer is that it is relatively inert, thus acting conservatively. If a constant sediment accumulation rate is assumed, down-core profiles of ash and pumice concentration will depend only on the details of bioturbational mixing. Modelling such profiles allows different bioturbation schemes to be evaluated.

Table 3-1 details a number of deep-sea sediment cores taken from the Pacific and Indian oceans where down-core concentrations of (62-125 $\mu$m) volcanic ash and pumice have been measured [*Ruddiman et al.*, 1980]. The sediment module is run once for each of these cores with bulk-matter deposition fluxes chosen to give the appropriate observed sediment accumulation rate. After sediment 'spin-up', an impulse addition of a 'colour' tracer (representing the input of volcanic material) is made to the sediment surface. Figure 3-2 shows the results of this exercise for the "10 cm only" and "5 cm plus deep mixing" mixing schemes. It can be seen that while the first scheme can reproduce tracer profiles in cores characterized by relatively high sedimentation rates (>2 cm $ka^{-1}$), it tends to over-estimate peak concentrations at lower rates. The second scheme, however, produces a reasonable fit under all sedimentation conditions. There is a general failure in both these and other schemes evaluated (not shown) to produce adequate mixing of tracer deeper than the level of impulse addition (the observed 'tail' to the right of the maximum tracer concentration). While prescribing stronger biodiffusion at depth can partly alleviate this mis-match it also seriously reduces peak concentrations. The inability to reproduce this feature highlights one of the deficiencies of a simple quasi-diffusional model, that of the role of non-local mixing events.

### *3.2.1.3 $^{14}C$ age profile simulation*

A second test of mixing scheme involves the use of down-core measurements made of $^{14}C$ age. Core ERDC-92 is chosen for this analysis, having already been extensively characterized in terms of mixing and accumulation regime by *Peng et al.* [1979]. The sediment sub-model is run assuming apparent (i.e., $^{14}C$ age-derived) sedimentation rates of 2.3 cm $ka^{-1}$ before 6 ka BP and 1.2 cm $ka^{-1}$, thereafter [*Peng et al.*, 1979]. No dissolution of $CaCO_3$ is prescribed, consistent with the shallow location of this core. $CaCO_3$ deposited to the

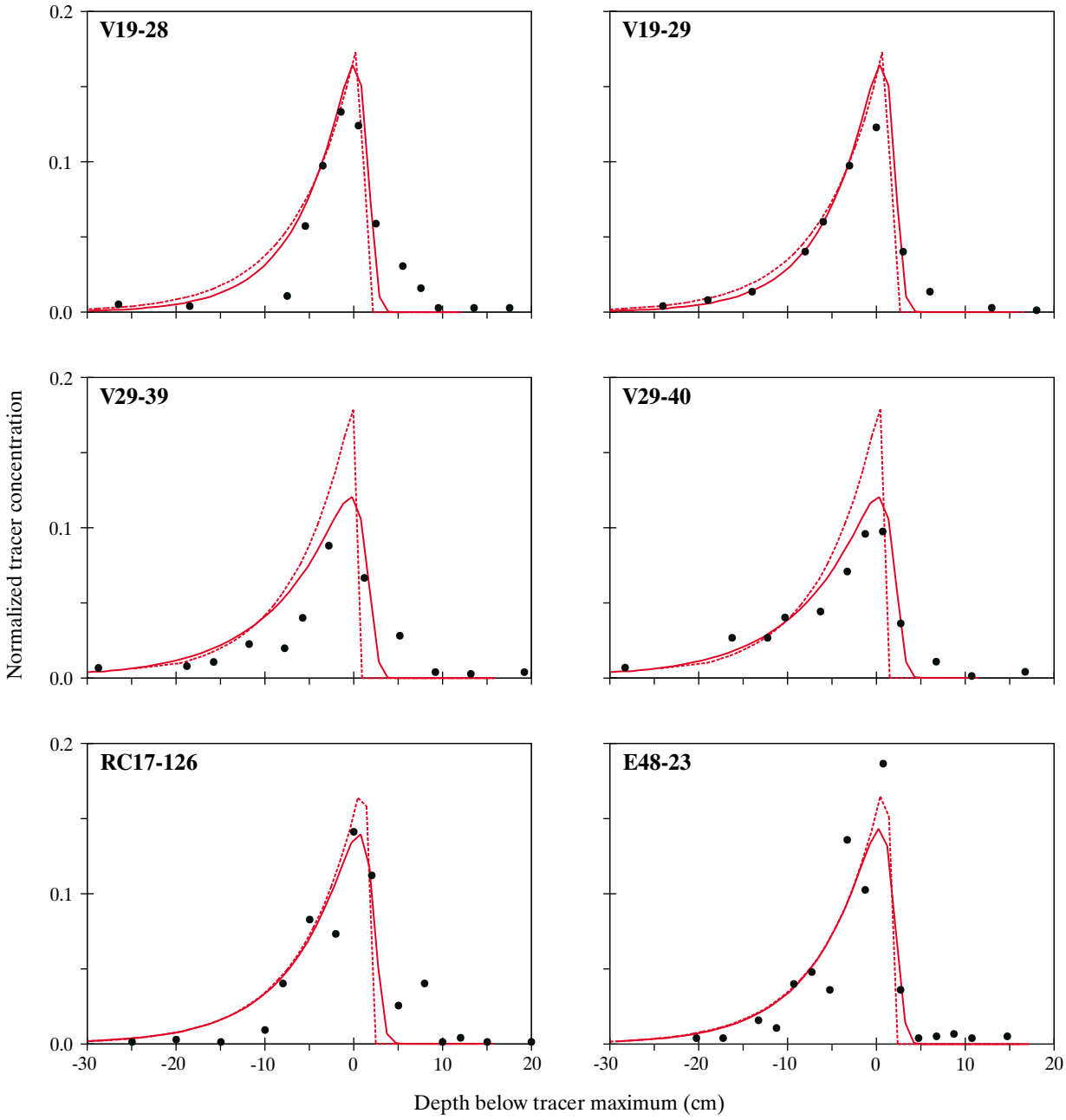


**Figure 3-2** Model down-core 'colour' tracer profiles (solid and dotted red lines, corresponding to the schemes "5 cm plus deep mixing" and "10 cm only", respectively) compared to observed ash and pumice concentrations (filled circles). All tracer concentrations are shown normalized to unit integrated volume.

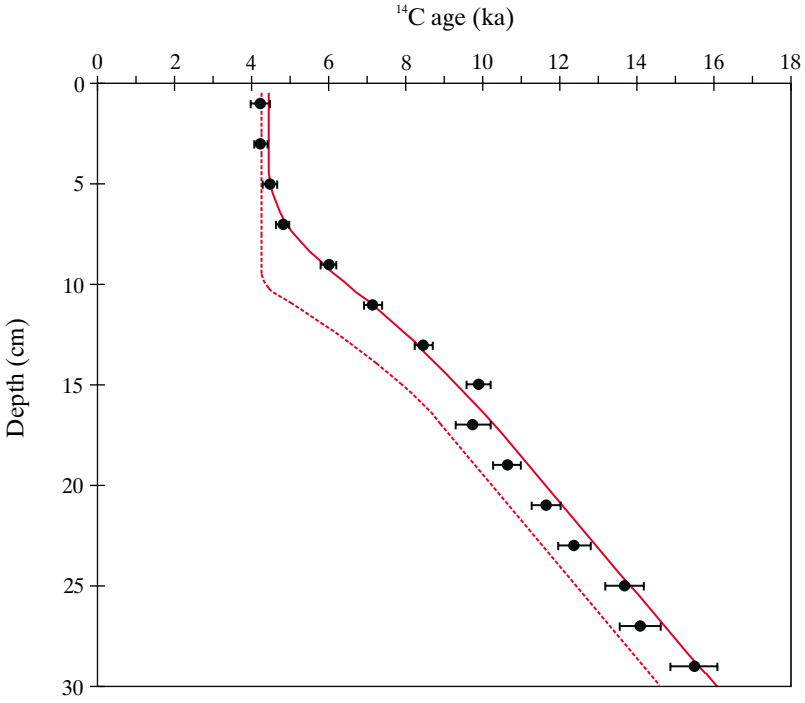


**Figure 3-3** Model down-core $CaCO_3$ $^{14}C$ age tracer profiles (solid and dotted red lines, corresponding to the schemes "5 cm plus deep mixing" and "10 cm only", respectively) compared to observations from core ERDC-92 [*Peng et al.*, 1979] (filled circles with error bars).

sediment surface in the model is assigned a $^{14}C$ age of 0.4 ka, in order to account for surface water aging [*Keir and Michel*, 1993; *Oxburgh*, 1998; *Peng et al.*, 1979]. The results from the same two bioturbation schemes as presented before are shown in Figure 3-3, and compared to observations. While both correctly reproduce the observed core-top $^{14}C$ age, the simple "10 cm only" scheme is noticeably less successful in reproducing the deeper age profile.

The "5 cm plus deep mixing" scheme is also evaluated against four $^{14}C$ profiles presented by *Broecker et al.* [1991], with corrections made for the surface ocean $^{14}C$ reservoir age as before. Core details, including apparent accumulation rates used to constrain the sediment module are listed in Table 3-2. The results of this exercise are shown in Figure 3-4, demonstrating that the mixing scheme is able to capture core-top $^{14}C$ ages and down-core profile of core FAM527-3, while introducing only a relatively small age offset (~0.5 ka) in cores EN66-21 and ERDC-92. However, the model significantly under-predicts $^{14}C$ ages in TT154-5. This apparently somewhat mixed success might be a direct consequence of the different oceanographic locations of the cores; while the other three cores come from either relatively shallow depths or from the Atlantic, TT154-5 is from the mid-depth Pacific. As such, it is likely to be bathed in water under-saturated with respect to $CaCO_3$ [*Archer*, 1996a]. A significant fraction of the (young $^{14}C$ age) $CaCO_3$ rain is therefore likely to dissolve upon reaching the surface and before being incorporated into the well-mixed layer, leading

**Table 3-2 Radiocarbon Profile Sediment Core Details**

| Core | Latitude | Longitude | Depth (m) | Sediment accumulation rate (cm ka$^{-1}$) | Reference |
|---|---|---|---|---|---|
| FAM527-3 | 36.8°N | 33.3°W | 2600 | 2.9 | *Nozaki et al.* [1977] |
| ERDC-92 | 2.2°S | 157.0°E | 1598 | 1.8 | *Berger and Killingley* [1982], *Peng et al.* [1979] |
| EN66-21 | 4.2°N | 20.6°W | 3995 | 1.4 | *DuBois and Prell* [1988] |
| TT154-5 | 10.3°S | 111.3°W | 3225 | 0.8 | *Broecker et al.* [1991] |

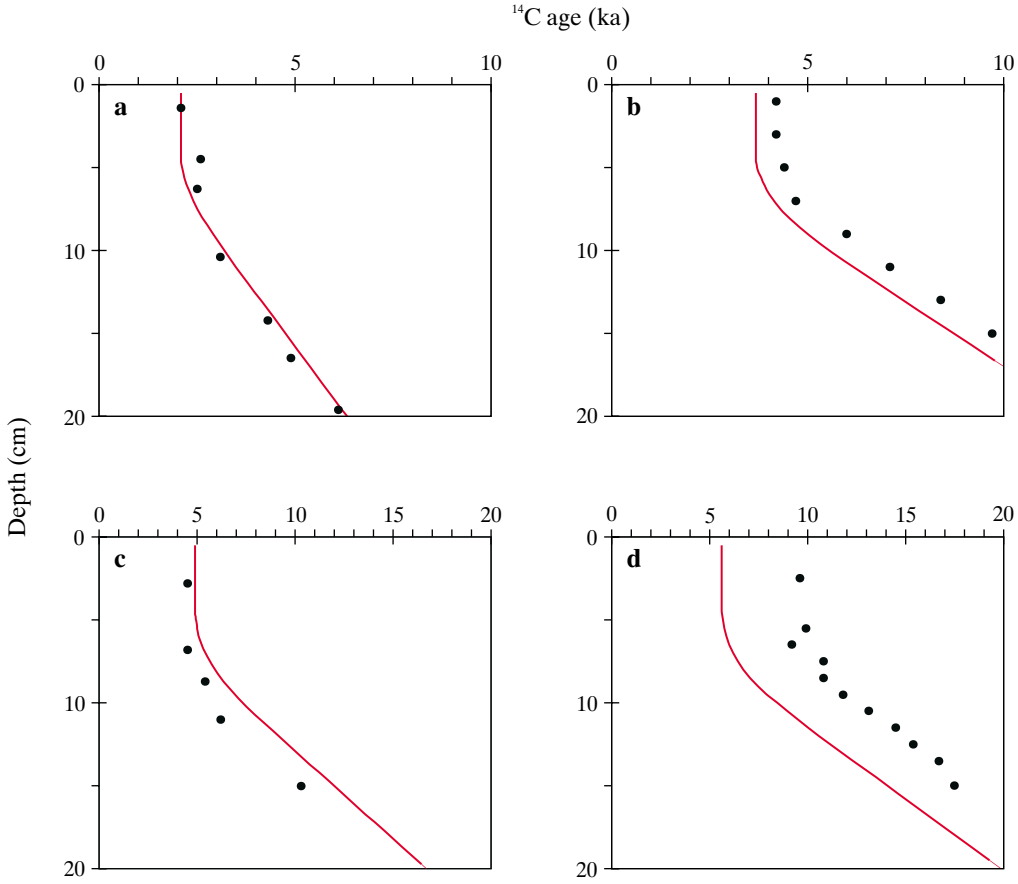


**Figure 3-4** Model down-core $CaCO_3$ $^{14}$C age tracer profiles (solid red lines, corresponding to the scheme "5 cm plus deep mixing") compared to observations from cores FAM527-3 (a), ERDC-92 (b), EN66-21 (c), and TT154-5 (d), all designated by filled circles.

to a higher-than expected $^{14}$C age [*Broecker et al.*, 1991, 1999b; *Oxburgh*, 1998]. That the simple test used here assumes that no dissolution of $CaCO_3$ takes place is the probable cause of this discrepancy. A secondary effect contributing to model-observation mismatch may be insufficient elapsed time since the LGM for a new steady-state to have been established. This is supported by an anti-correlation between the degree of $^{14}$C age mis-match and sediment accumulation rate. Only for the fastest sediment accumulation rate (FAM527-3) would it have been possible for virtually all trace of LGM conditions to have been erased over the entire depth of the observed profile.

#### *3.2.1.4 Scheme choice*

Although carrying an additional computational burden associated with it, the "5 cm plus deep mixing" scheme appears to perform better than the simpler "10 cm only" parameterization. However, the performance of both of these is significantly better than that of other schemes tested, such as the power law mixing parameterization of *Walker and Opdyke* [1995]. The "5 cm plus deep mixing" scheme is therefore adopted as default in SUE. Although some models have introduced a dependence of sediment mixing rates on ocean depth or POM rain rates [*Archer et al.*, in press; *Muhoven and Francois*, 1996], the chosen parameterization is applied uniformly to all sediments throughout the model ocean as an initial step.

### 3.2.2 Porosity

The porosity of deep-sea sediments can affect diagenetic behaviour through scaling the vertical accumulation rates (which in turn determines the mean time spent by material in the sub-surface zone of intense diagenetic alteration), and by controlling the diffusivity of dissolved species within the sediment matrix. Although there appears to be some dependence of porosity on sediment composition [*Archer et al.*, 1979; *Martin et al.*, 1991], for simplicity, a single empirically-derived sediment porosity profile is utilized in this study.

Figure 3-5 shows porosity profiles estimated from *in situ* microelectrode resistivity measurements in a number of

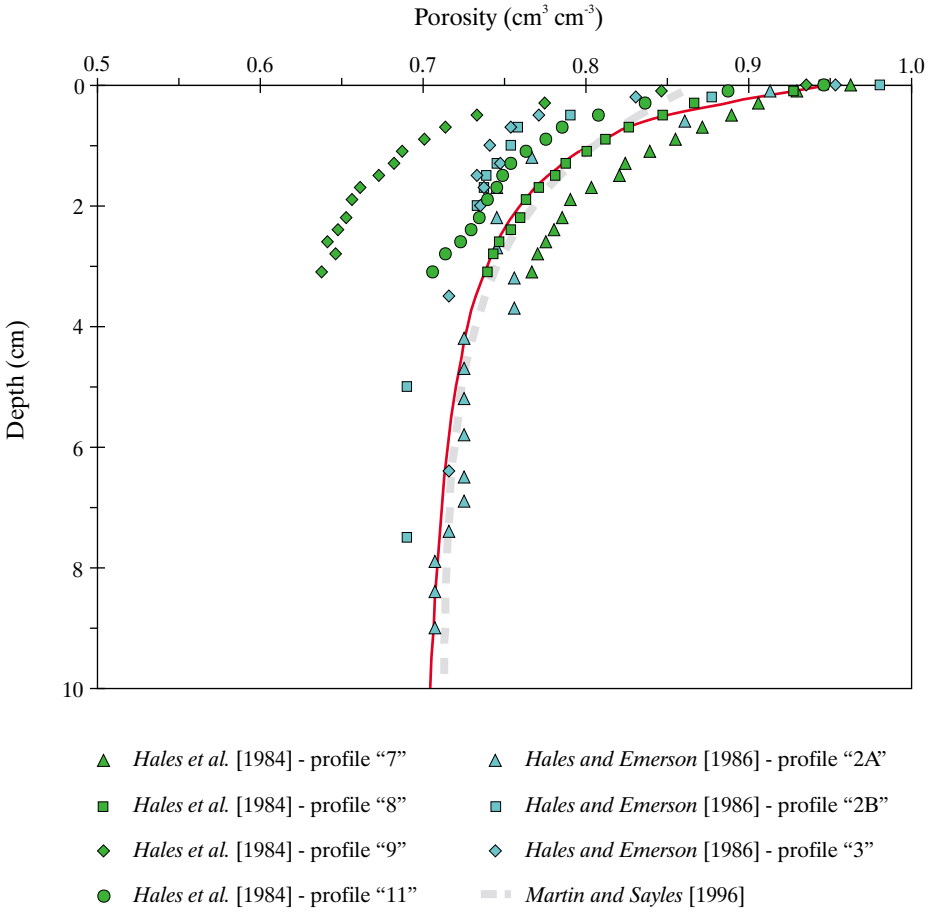


**Figure 3-5** Model sediment down-core porosity profile (continuous line) compared with observations.

equatorial Pacific [*Hales and Emerson*, 1996] and north Atlantic cores [*Hales et al.*, 1994], together with a mean equatorial Atlantic profile [*Martin and Sayles*, 1996]. Assuming porosities at the surface of 0.95 and 0.70 cm3 $cm^{-3}$ at depth, all these observations can be reasonably be described by

$$\phi_{(z)} = 0.69 + 0.26 \cdot (1.0 + z)^{-1.2} \qquad (3\text{-}5)$$

where $\phi_{(z)}$ is the porosity at depth $z$ (cm) in the sediment. This gives a mean porosity of ~0.89 $cm^3$ $cm^{-3}$ over the uppermost 0.5 cm, consistent with *Hensen et al.* [1998], and an overall profile similar to models use by *Heinze et al.* [1999] and *Jahnke et al.* [1997]. The 5 cm thick surface layer in the sediment module is therefore assigned a porosity of 0.776 $cm^3$ $cm^{-3}$, with 0.705 $cm^3$ $cm^{-3}$ applied uniformly to all sub-layers.

### 3.2.3 Numerical implementation of diagenesis

The diagenetic alteration of material in deep-sea sediments is in essence a 1-D reaction-diffusion system. Numerical stability considerations in the solution of such a system dictate a minimum time step for the required vertical resolution [*Moldrup et al.*, 1996] such that explicit application over a global scale for extended time model runs is problematic. While elegant schemes have been developed for rapid approximation of a quasi-steady solution [*Archer*, 1991, *Archer et al.*, in press], there are alternative methodologies for the efficient encapsulation of complex diagenetic behaviour.

On the basis of a set of simplifying assumptions, *Sigman et al.* [1998] successfully reduced the dimensionality of a complex model of $CaCO_3$ diagenesis to a system defined by only 2 independent variables. A multi-variate polynomial fit was derived from this and subsequently employed within a global carbon cycle model. However, if the number of variables considered essential for a reasonable representation of system behaviour exceeds this, it becomes difficult to construct an equivalent regression surface. Alternatively, a representation of the solution surface can be obtained by training a neural network on the underlying numerical model. Unfortunately, the protracted 'training' times required by neural networks will tend to curtail their use where the parameter space is large. A simple 'look-up' table approach is therefore introduced here for the

representation of sedimentary diagenetic behaviour, whereby required values of state are obtained through linear interpolation on a regular grid of pre-calculated values within an *n*-dimensional space, where *n* is the number of parameters defining the system.

### 3.2.4 Sedimentary diagenesis of $CaCO_3$

Sedimentary diagenesis of $CaCO_3$ follows *Archer* [1991]. In this model, the dissolution of $CaCO_3$ within a 10 cm thick surface zone is considered, driven both by the overlying ocean chemistry and as a result of remineralization of POC within the sediments. The assumption is made that POC reaching the sediments is completely reduced under oxic conditions. Numerical solution is achieved via a relaxation method within a vertically discretized system. While no account is taken of anoxic conditions produced at depth or resulting from a high ratio of POC rain rate to ocean dissolved oxygen concentrations, this scheme has proved successful in a number of previous global carbon cycle models [*Archer*, 1996a; *Archer et al.*, 1998; *Heinze et al.*, 1999]. For application in SUE, several minor modifications are made. Firstly, to ensure internal model consistency, the same representation of carbonate chemistry as that of the oceanic component is used (Appendix I). Secondly, a single down-core porosity is assumed, independent of sediment composition (3.2.2).

#### *3.2.4.1 Look-up table implementation*

In the *Archer* [1991] model, $CaCO_3$ dissolution flux density across the sediment-water interface ($fdis^{CaCO_3}$) is primarily a function of ocean depth ($D$), the bottom-water concentration of total dissolved inorganic carbon ([DIC]), alkalinity ([ALK]), and dissolved oxygen ($[O_2]$), the mass fraction of $CaCO_3$ in the sediments ($c^{CaCO_3}$), and the flux density of particulate organic matter delivered to the sediment surface ($fsed^{POC}$). The look-up table function for such as system can be written

$$fdis^{CaCO_3} = \mathrm{L}\left( D,[\mathrm{DIC}],[\mathrm{ALK}],c^{CaCO_3},[O_2],fsed^{POC} \right) \quad (3\text{-}6)$$

where L is a function for linear interpolation within an *n*-dimensional space. However, the six-dimensional space defined by these variables does not easily yield a manageable look-up table. Parameter space dimensionality can be reduced considering that it is carbonate ion concentration that directly determines $CaCO_3$ dissolution rates rather than DIC and ALK individually. A variable representing the degree of under-saturation ($d\mathrm{CO}_3$) is therefore introduced following *Sigman et al.* [1998], defined as the difference between ambient $[CO_3^{2-}]$ and the local saturation value for $CaCO_3$. The spanning space is collapsed through the substitution of [DIC] and [ALK] by a single descriptive variable ($d\mathrm{CO}_3$)

$$fdis^{CaCO_3} = \mathrm{L}\left( D,d\mathrm{CO}_3,c^{CaCO_3},[O_2],fsed^{POC} \right) \quad (3\text{-}7)$$

A further dimensional reduction is made by assuming a uniform dissolved oxygen concentration throughout the ocean (taken to be 200 $\mu$mol $kg^{-1}$). This is justified on the basis of the relatively weak dependence of $fdis^{CaCO_3}$ on $[O_2]$ under typical benthic conditions (of order 0.01% ($\mu$mol $kg^{-1})^{-1}$). The $CaCO_3$ dissolution flux density is now a much simpler function of just four variables;

$$fdis^{CaCO_3} = \mathrm{L}\left( D,d\mathrm{CO}_3,c^{CaCO_3},fsed^{POC} \right) \quad (3\text{-}8)$$

The spanning set of look-up table parameters are detailed in Table 3-3. Spanning ranges are generally chosen to cover conditions found in the benthic environment, with step intervals relaxed where $fdis^{CaCO_3}$ is only weakly non-linear with a particular parameter.

Since both forms of biogenic $CaCO_3$ are resolved in SUE two look-up tables must be generated, one for calcite and the other for aragonite. For the dissolution of calcite, parameter values are taken from *Archer* [1996a] for the order of dissolution (4.5) and dissolution rate constant (1.0 $d^{-1}$). The dissolution rate constant for aragonite is assumed to be the same, but a slightly lower value of 4.2 is used for the reaction order [*Keir*, 1980]. Artificially separating the dissolution of calcite and aragonite in this way presents the problem of how dissolution forcing due to POC remineralization is partitioned between the two polymorphs. As a crude approximation $fsed^{POC}$ is split between the calcite and aragonite diagenetic systems in proportion to their relative mass abundance in the sediments, giving

$$fdis^{cal} = \mathrm{L}\left( D,d\mathrm{CO}_3^{cal},c^{cal},\frac{c^{cal}}{c^{cal}+c^{arg}}\cdot fsed^{POC} \right) \quad (3\text{-}9a)$$

$$fdis^{arg} = \mathrm{L}\left( D,d\mathrm{CO}_3^{arg},c^{arg},\frac{c^{arg}}{c^{cal}+c^{arg}}\cdot fsed^{POC} \right) \quad (3\text{-}9b)$$

#### *3.3.4.2 The location of $CaCO_3$ dissolution*

In terms of $CaCO_3$ mass balance it makes no difference from where in surface sediments material is dissolved. However, this is not true for qualities of $CaCO_3$ that may vary with time such as $^{13}C$ and $^{14}C$ isotopic composition. A number of different end-member models have been proposed to qualitatively describe the effect of dissolution on such properties [*Broecker et al.*, 1991; *Oxburgh and Broecker*, 1993], namely; "interface" dissolution, where the dissolution of settling $CaCO_3$ takes place in the surficial fluff layer before any downwards mixing occurs; "homogeneous" dissolution, where settling $CaCO_3$ is first homogenized into the intensely bioturbated zone prior to dissolution; and "sequential" or

**Table 3-3** $CaCO_3$ Diagenesis Look-up Table Spanning Set

| Parameter | Spanning range | Spanning step | Units |
|---|---|---|---|
| $dCO_3$ | -100 to 100 | 1 | $\mu$mol $kg^{-1}$ |
| $D$ | 0 to 10000 | 1000 | m |
| $fsed_{POC}$ | 0 to 50 | 1 | $\mu$mol $cm^2$ $a^{-1}$ |
| $c_{CaCO_3}$ | 10 to 100 | 10 | % |

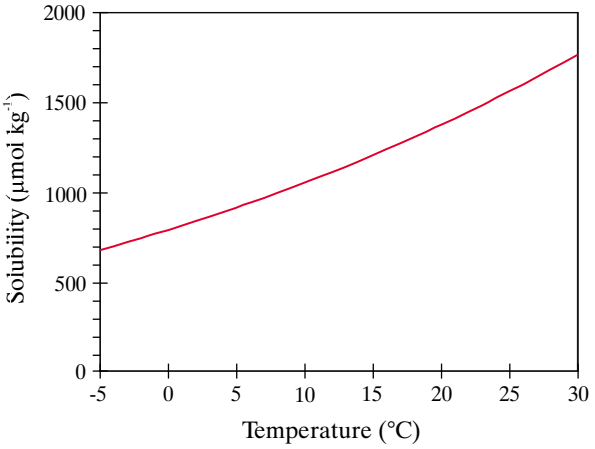


**Figure 3-6** Dependence of opal solubility on temperature [*Van Cappellen and Qiu*, 1997a].

"one pass" dissolution, where $CaCO_3$ is initially mixed into the surface layer, but 'ages', becoming less susceptible to dissolution with time. On the basis of observed $^{14}C$ ages, interface dissolution of $CaCO_3$ has generally been considered to be the dominant process [*Broecker et al.*, 1991, 1999b; *Keir and Michel*, 1993; *Oxburgh and Broecker*, 1993; *Oxburgh*, 1998] although there has been some recent support for the action of an ageing-like process [*Martin et al.*, 2000]. Dissolution of $CaCO_3$ within the sediment module is therefore assumed to take place before mixing into the surface zone occurs according to the 'interface' dissolution model. If the dissolution flux is less than the rain flux, the remaining material is then incorporated into the surface mixed layer, while if the dissolution flux is greater than the rain flux additional material is removed from the mixed layer to make up this shortfall (up to a volume equal to the entire $CaCO_3$ surface layer inventory if necessary).

## 3.2.5 Sedimentary diagenesis of biogenic opal

Despite its importance to both the dynamics of the global carbon cycle and in the interpretation of paleoceanographic proxies of past change, the factors determining the preservation of opal in deep-sea sediments are poorly understood [*Archer et al.*, 1993]. As a result, there have been few previous global carbon cycle models in which the ocean Si cycle has been comprehensively represented [*Archer et al.*, 2000; *Heinze et al.*, 1999]. A new description of sedimentary opal diagenesis is presented here, developed empirically from recent observations and laboratory analyses of opal dissolution and thermodynamics in a series of cores taken from the Southern Ocean [*Rabouille et al.*, 1997; *Van Cappellen and Qui*, 1997a,b].

### *3.2.5.1 A model for sedimentary opal diagenesis*

The system for the diagenetic alteration of opal within deep-sea sediments can be restricted to the uppermost 10 cm since little net diffusion of $H_4SiO_4$ is observed below this depth [*Rabouille et al.*, 1997; *Sayles et al.*, 1996; *Van Bennekom et al.*, 1988]. A further simplifying assumption is made in that the concentration of opal is constant with depth, again in line with observations [*Rabouille et al.*, 1997; *Schluter and Sauter*, 2000; *Van Bennekom et al.*, 1988]. The system is vertically discretized into 0.2 cm thick sub-layers with down-core sediment porosity following (3-5), and solved on a finite-difference basis. However, considering that the relaxation time of solutes in the system is several orders of magnitude faster than for the solids [*Rabouille and Gaillard*, 1990], pore-water $H_4SiO_4$ concentrations are solved for in isolation. Steady-state is assumed to have been obtained when the dissolution flux across the sediment-water interface changes by less than 0.001% between time steps. The two individual components of the reaction-diffusion system are defined as follows.

*Diffusion of* $H_4SiO_4$

Correcting for tortuosity [*Ullman and Aller*, 1982] the *in situ* diffusion of $H_4SiO_4$ at depth $z$ in the sediment is described by

$$D_{\mathrm{sed}(z)} = \left(\phi_{(z)}\right)^{(n-1)} \cdot D_{\mathrm{SW}} \qquad (3\text{-}10)$$

where $D_{\mathrm{SW}}$ in the molecular diffusivity of $H_4SiO_4$ in free seawater, taken as $4.59\times10^{-6}$ cm$^2$ s$^{-1}$ at 0°C and adjusted for the actual bottom-water temperature after *Hensen et al.* [1998]

$$D_{\mathrm{SW}} = 4.59\times10^{-6} + 1.74\times10^{-7}\cdot(T_{\mathrm{SW}} - 273.15) \qquad (3\text{-}11)$$

where $T_{\mathrm{SW}}$ is the temperature of the bottom-water (K), $\phi_z$ is the porosity at depth $z$ (3-5), and $n$ is a correlation factor taking a value of 2.5 typical for deep-sea sediments [*Hensen et al.*, 1998; *Ullman and Aller*, 1982]. Compared with molecular diffusion of $H_4SiO_4$, bioturbation and advection (due to sediment accumulation) play no significant role in aqueous transport within the sediment [*Schink et al.*, 1975] and are thus omitted.

*Dissolution of biogenic opal*

Dissolution of opal (in units of mol cm$^{-3}$ opal a$^{-1}$) at depth $z$ in the sediment proceeds according to

$$R^{\mathrm{opal}}_{(z)} = k^{\mathrm{opal}}_{(z)} \cdot \rho^{\mathrm{opal}} \cdot [1 - \phi_{(z)}] \cdot c^{\mathrm{opal}}_{(z)} \qquad (3\text{-}12)$$

where $k^{\mathrm{opal}}_{(z)}$ is a dissolution rate constant (a$^{-1}$), $\rho^{\mathrm{opal}}$ the density of opal (mol cm$^{-3}$), $\phi_{(z)}$ sediment porosity (cm$^3$ cm$^{-3}$), and $c^{\mathrm{opal}}_{(z)}$ the solid fraction of opal (cm$^3$ cm$^{-3}$) as a proportion of sediment solids. Traditionally, opal dissolution rate has been assumed to be a linear function of the degree of under-saturation [*Archer et al.*, 1993, 2000; *Rabouille and Gaillard*, 1990; *Rabouille et al.*, 1997; *Schink et al.*, 1975]

$$k^{\mathrm{opal}}_{(z)} = a \cdot u^{\mathrm{opal}}_{(z)} \qquad (3\text{-}13)$$

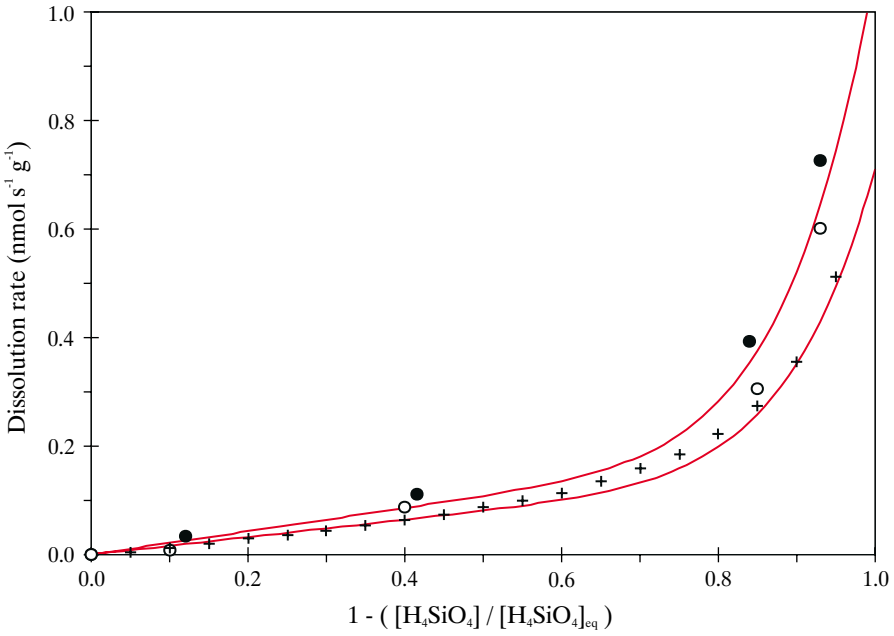


**Figure 3-7** Opal dissolution rate as a function of degree of under-saturation ($u^{\mathrm{opal}}$). Directly measured (at 5°C) dissolution rates are shown as filled (for core KYB05) and unfilled (KTB06) circles, respectively, together with estimated (at 0°C) dissolution rates marked by crosses [*Van Cappellen and Qiu*, 1997b]. Calculated dissolution rates using (3-16) are shown for temperatures of 5°C (top line) and 0°C (bottom line).

where $a$ is a constant and $u_{(z)}^{\mathrm{opal}}$ is the degree of local pore-water under-saturation with respect to the solid phase

$$u_{(z)}^{\mathrm{opal}} = \frac{[\mathrm{H_4SiO_4}]_{\mathrm{eq}(z)}^{\mathrm{opal}} - [\mathrm{H_4SiO_4}]_{(z)}}{[\mathrm{H_4SiO_4}]_{\mathrm{eq}(z)}^{\mathrm{opal}}} \qquad (3\text{-}14)$$

where $[\mathrm{H_4SiO_4}]_{(z)}$ is the pore water concentration of silicic acid and $[\mathrm{H_4SiO_4}]_{\mathrm{eq}(z)}^{\mathrm{opal}}$ the equilibrium (saturation) concentration with respect to opal. $[\mathrm{H_4SiO_4}]_{\mathrm{eq}(z)}^{\mathrm{opal}}$ can be estimated empirically [*Van Cappellen and Qiu*, 1997a] by

$$\log_{10}\left([\mathrm{H_4SiO_4}]_{\mathrm{eq}(z)}^{\mathrm{opal}}\right) = 6.44 - \frac{968}{T} \qquad (3\text{-}15)$$

where $T$ is the absolute temperature (Figure 3-6). Although a dependence of $[\mathrm{H_4SiO_4}]_{\mathrm{eq}(z)}^{\mathrm{opal}}$ on *p*H has also been observed [*Van Cappellen and Qiu*, 1997a], errors arising from omission of this effect are unlikely to be more than ~5% under typical pore-water conditions.

Contrary to the common assumption of linear dissolution kinetics (3-13) *Van Cappellen and Qiu* [1997b] found that the relationship describing dissolution rate appeared to become highly nonlinear as $u^{\mathrm{opal}}$ approached unity. As shown in Figure 3-7, estimated and directly observed dissolution rates [*Van Cappellen and Qiu*, 1997b] can be crudely represented by an equation of the form

$$R^{\mathrm{opal}} = 0.16 \cdot \left(1 + \frac{T}{15}\right) \cdot u^{\mathrm{opal}} + 0.55 \cdot \left(\left(1 + \frac{T}{400}\right)^4 \cdot u^{\mathrm{opal}}\right)^{9.25} \qquad (3\text{-}16)$$

where $R^{\mathrm{opal}}$ is the dissolution rate of opal (in units of nmol $s^{-1}$ $g^{-1}$) and $T$ is the temperature (°C). Although this function is wholly *ad hoc*, it is consistent with available data over a range in $T$ and $u^{\mathrm{opal}}$ that spans typical abyssal conditions. It is also characterized by a $Q_{10}$ of 2.3 consistent with *Kamatani* [1982] and can thus be expected to have useful predictive power over a much wider range of (temperature) conditions. A scaling factor $\eta_{\mathrm{l}\,(z)}^{\mathrm{opal}}$ accounting for the relative change in dissolution rate due to deviations in ambient temperature from 0°C and zero silicic acid concentration (i.e., completely under-saturating) is derived by normalizing (3-16) to a value of unity at $T$ = 0°C and $u_{(z)}^{\mathrm{opal}} = 1$

$$\eta_{\mathrm{l}\,(z)}^{\mathrm{opal}} = 0.225 \cdot \left(1 + \frac{T}{15}\right) \cdot u_{(z)}^{\mathrm{opal}} + 0.775 \cdot \left(\left(1 + \frac{T}{400}\right)^4 \cdot u_{(z)}^{\mathrm{opal}}\right)^{9.25} \qquad (3\text{-}17)$$

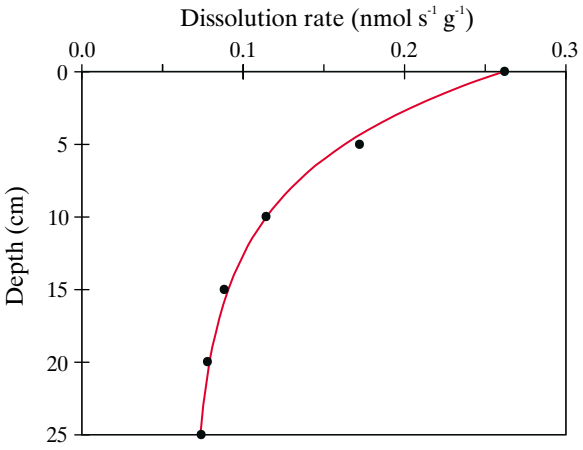


**Figure 3-8** Down-core decrease in opal dissolution rate (at half-saturation). Observed data (filled circles) from *Van Cappellen and Qui* [1997b] along with model fit (3-18).

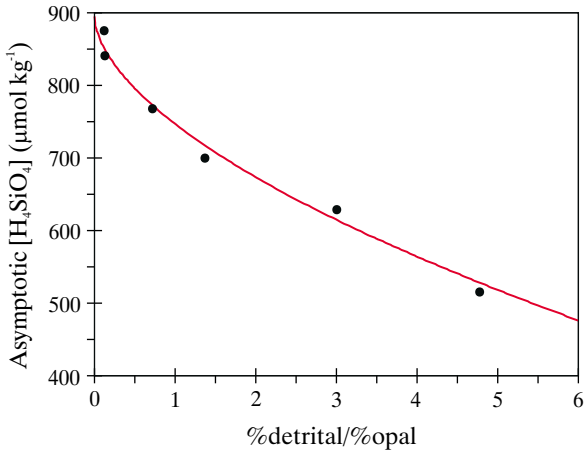


**Figure 3-9** Dependence of $[H_4SiO_4]_{asym}$ on the ratio of detrital to opal sediment content; observed data (filled circles) from *Van Cappellen and Qui* [1997a] along with model fit (3-20).

Early diagenetic alteration of opal also appears to affect dissolution rates, with rate constants inversely correlated with depth in the sediment [*Van Cappellen and Qiu*, 1997b] (Figure 3-8). This can be approximated

$$R^{opal} = 0.068 + 0.194 \cdot e^{\left(\frac{-z}{7.0}\right)} \qquad (3\text{-}18)$$

Normalizing to a value of unity at the sediment surface (i.e., before any additional diagenetic alteration has occurred) gives a second scaling factor

$$\eta_{2(z)}^{opal} = 0.26 + 0.74 \cdot e^{\left(\frac{-z}{7.0}\right)} \qquad (3\text{-}19)$$

The introduction of this factor is analogous to the decrease in kinetic 'constant' with depth employed by *Rabouille et al.* [1997].

Diagenetic effects also appear to suppress solubility. *Van Bennekom et al.* [1988] found that low concentrations of Al markedly lower the solubility of biogenic and amorphous silica, with opal samples exhibiting a contraction of the lattice at relatively high Al/Si ratios suggesting a degree of substitution of Si by Al. This is supported by observations made by *Van Cappellen and Qiu* [1997a] regarding the asymptotic concentration of pore-water silicic acid ($[H_4SiO_4]_{asym}$) reached in the sediment. They noted that $[H_4SiO_4]_{asym}$ correlated with the mass ratio of detrital material to opal, suggesting that interstitial incorporation of Al into opal surface layers during a process of continuous dissolution/recrystalization might lead to decreasing solubility. Reduction in $[H_4SiO_4]_{asym}$ with the ratio of detrital to opal content [*Van Cappellen and Qiu*, 1997a] (Figure 3-9) can be approximated

$$[H_4SiO_4]_{asym} = 895 - \left(5528 \cdot \frac{c^{detrital}}{c^{opal}}\right)^{0.58} \qquad (3\text{-}20)$$

where $c^{detrital}$ and $c^{opal}$ are the fractions (wt%) of detrital material and opal in the sediment, respectively. Although the highest sediment core %detrital/%opal ratio considered by *Van Cappellen and Qiu* [1997a] was 4.8 (corresponding to a reduction in $[H_4SiO_4]_{asym}$ from ~880 to ~520 $\mu$mol kg$^{-1}$) values of $[H_4SiO_4]_{asym}$ as low as 150 to 300 $\mu$mol kg$^{-1}$ have been observed in opal-poor cores outside of the Southern Ocean [*Archer et al.*, 1993; *Martin et al.*, 1991; *McManus et al.*, 1995]. The observed relationship is therefore extrapolated to a maximum %detrital/%opal ratio of 15, producing a potential minimum $[H_4SiO_4]_{asym}$ value of around 180 $\mu$mol kg$^{-1}$ under typical abyssal temperatures. Despite the dependence of asymptotic silicic acid concentrations on sediment composition being accountable on a purely kinetic basis [*Rabouille et al.*, 1997], to reduce the degrees of freedom in the model the assumption is made that the equilibrium saturation state of opal is directly affected (i.e., $[H_4SiO_4]_{eq}^{opal}$). A reduction factor ($\gamma_{Al}$) accounting for Al-inhibition is then defined

$$\gamma_{Al} = 0.2 \qquad \frac{c^{detrital}}{c^{opal}} > 15 \qquad (3\text{-}21a)$$

$$\gamma_{Al} = 1.0 - \left(0.045 \cdot \frac{c^{detrital}}{c^{opal}}\right)^{0.58} \qquad \frac{c^{detrital}}{c^{opal}} \le 15 \qquad (3\text{-}21b)$$

and used to modify $[H_4SiO_4]_{eq(z)}^{opal}$ (3-15), to give

$$[H_4SiO_4]_{eq(z)}^{opal} = \gamma_{Al} \cdot 10^{\left(6.44 - \frac{968}{T_{(z)}}\right)} \qquad (3\text{-}22)$$

A full description for the dissolution rate of opal within the sediments can now be written

$$R_{(z)}^{\text{opal}} = \eta_{1(z)}^{\text{opal}} \cdot \eta_{2(z)}^{\text{opal}} \cdot k_0^{\text{opal}} \cdot \rho^{\text{opal}} \cdot [1-\phi_{(z)}] \cdot c_{(z)}^{\text{opal}} \quad (3\text{-}23)$$

where $k_0^{\text{opal}}$ is the dissolution rate constant ($a^{-1}$) for 'fresh' opal delivered to the sediment surface (i.e., in a diagenetically unaltered state) under conditions of complete under-saturation and at a temperature of 0°C. All that remains is then to determine a value for $k_0^{\text{opal}}$. Unfortunately, published estimates for the dissolution rate constant of opal vary widely. Model fitting of a series of Antarctic cores suggests a value at the sediment surface in the range 0.016 to 0.315 $a^{-1}$ [*Rabouille et al.*, 1997]. *Schink et al.* [1975] adopted a value of 0.032 $a^{-1}$, but noted that experimental determinations often give much higher values than this, upwards of 0.063 - 0.252 $a^{-1}$. A further complication arises in that all these estimates are based on the assumption of linear kinetics.

The value of $k_0^{\text{opal}}$ is therefore optimized to reproduce (under equivalent conditions) estimated opal dissolution fluxes across the sediment-water interface ($fdis^{\text{opal}}$) of each of a series of Southern Ocean cores [*Rabouille et al.*, 1997]. To achieve this, the model was run for each of the cores detailed in Table 3-4, taking opal and detrital content from observations and assuming a bottom-water $H_4SiO_4$ concentration of 145 $\mu$mol $kg^{-1}$ typical of that area [*Conkright et al.*, 1994]. Since laboratory analyses on these cores were carried out at relatively elevated temperatures (2 to 4°C) compared to the abyssal Southern Ocean [*Rabouille et al.*, 1997] and there being a general likelihood of post-recovery distortion in $[H_4SiO_4]$ profile [*Martin et al.*, 1991; *McManus et al.*, 1995], the adoption of a temperature characteristic of the benthic location may not necessarily be appropriate. Instead, an effective temperature of 3.5°C is assumed, giving good agreement between observed values of $[H_4SiO_4]_{\text{asym}}$ [*Rabouille et al.*, 1997] and $[H_4SiO_4]_{\text{eq}}^{\text{opal}}$ predicted by (3-15). However, even accounting for all these factors the estimated value of $k_0^{\text{opal}}$ still ranges from 0.07 to 0.3 $a^{-1}$. That these are all significantly lower than suggested by the kinetic experiments of *Van Cappellen and Qiu* [1997b] made on samples taken from the same cores (0.66 nmol $s^{-1}$ $g^{-1}$, equivalent to 1.25 $a^{-1}$) may be due to further differences between experimental and *in situ* conditions. It is likely that opal isolated from a sedimentary matrix behaves in a thermodynamically different manner from that still in the presence of detrital material, so that care must be taken in the interpretation of laboratory analyses.

On the basis that the presence of detrital material appears to exert an important control on asymptotic silicic acid concentrations (Figure 3-9) $k_0^{\text{opal}}$ is made a function of the %detrital/%opal ratio. The relationship is defined consistent with the individually fitted core-specific dissolution rates (Table 3-4). An additional constraint is imposed of a value of 1.25 $a^{-1}$ at a %detrital/%opal ratio of 0.0, assuming that the kinetic experiments of *Van Cappellen and Qiu* [1997b] are representative of conditions where there is no detrital matter influence. This gives rise to the relationship (Figure 3-10)

$$k_0^{\text{opal}} = 0.05 + 0.055 \cdot \left( 0.0164 + \frac{c^{\text{detrital}}}{c^{\text{opal}}} \right)^{-0.75} \quad (3\text{-}24)$$

### *3.2.5.2 Look-up table implementation*

In an analogous manner to that for $CaCO_3$, the sedimentary diagenesis of opal in SUE is represented via means of a look-up table. The spanning set of parameters utilized for this are shown in Table 3-5. As before, these represent something of a compromise between the dimensionality and resolution of the parameter space describing the processes, and considerations of computational resource availability.

A look-up table function is defined for the $H_4SiO_4$ flux density across the sediment-ocean interface resulting from opal dissolution within the sediment

$$fdis^{H_4SiO_4} = L\left(T, [H_4SiO_4], c^{\text{opal}}, c^{\text{detrital}}\right) \quad (3\text{-}25)$$

where $T$ and $[H_4SiO_4]$ are the bottom-water temperature and silicic acid concentrations, respectively, while $c^{\text{opal}}$ and

**Table 3-4** Details of Sediment Core Observations Together With Fitted Model Dissolution Flux ($fdis^{\text{opal}}$)

| Core ID | opal (wt%) | $CaCO_3$ (wt%) | detrital (wt%) | $\frac{\text{wt\%detrital}}{\text{wt\%opal}}$ | $[H_4SiO_4]_{\text{asym}}$ [1] ($\mu$mol $kg^{-1}$) | $fdis^{\text{opal}}$ [1] ($\mu$mol $cm^{-2}$ $a^{-1}$) | $[H_4SiO_4]_{\text{asym}}$ [2] ($\mu$mol $kg^{-1}$) | $fdis^{\text{opal}}$ [2] ($\mu$mol $cm^{-2}$ $a^{-1}$) | $k_0^{\text{opal}}$ [2] ($a^{-1}$) |
|---|---|---|---|---|---|---|---|---|---|
| KTB05 | 75.5 | 12.8 | 9.2 | 0.12 | 875 | 132.0 | 835 | 146.3 | 0.293 |
| KTB06 | 86.3 | 0.3 | 10.8 | 0.13 | 841 | 203.0 | 834 | 154.0 | 0.288 |
| KTB11 | 36.7 | 33.8 | 26.5 | 0.72 | 768 | 66.0 | 761 | 65.4 | 0.119 |
| KTB19 | 38.0 | 7.7 | 52.2 | 1.37 | 700 | 53.5 [3] | 709 | 55.7 | 0.093 |
| KTB26 | 17.5 | 28.0 | 53.3 | 3.05 | 629 | 31.0 | 608 | 30.3 | 0.074 |
| KTB28 | 15.8 | 7.7 | 75.5 | 4.78 | 515 | 24.0 | 526 | 23.9 | 0.067 |

[1] *Rabouille et al.* [1997]
[2] model fitted (present study)
[3] estimated

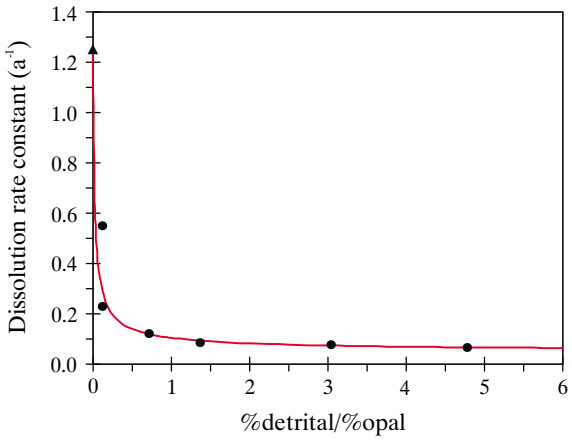


**Figure 3-10** Dependence of $k_0^{opal}$ on the ratio of detrital to opal sediment content. Model dissolution rates required to produce the estimated dissolution fluxes of *Rabouille et al.* [1997] are shown as filled circles, while the dissolution rate of free opal under ambient conditions of 0°C and complete under-saturation estimated from *Van Cappellen and Qiu* [1997b] is shown as a filled triangle.

$c^{detrital}$ are the (mass) fractions of the opal and detrital material in the sediment surface layer, respectively.

### 3.2.5.3 *Model validation*

The opal diagenesis model has been constructed empirically on studies utilizing cores taken from a single transect located in the Southern Ocean. It is therefore essential to validate the model against data from geographically, and more importantly, biogeochemically different locations. Rather than focus on the specifics of any one particular site for validation, since the diagenesis model is to be used within a global framework where only mean regional behaviour is under consideration, it is more appropriate to analyse general trends of response. A database of parameters having direct equivalence with model output is constructed (detailed in Appendix III), taken from studies carried out on cores located mainly in the tropical and sub-tropical Pacific and sub-tropical Atlantic. Conditions in these regions generally deviate substantially from those in the Southern Ocean, often characterized by much higher $CaCO_3$ sediment content (especially in the Atlantic), lower opal rain rates, higher (Pacific) or lower (Atlantic) silicic acid concentrations, and slightly warmer temperatures. Such data is thus able to provide a robust test of the model parameterization.

Model data is generated with SUE configured with the simple box structure, ocean circulation, and biological export production of the PANDORA box model [*Broecker and Peng*, 1986]. Remineralization of POM, $CaCO_3$, and opal takes place below the surface layer according to the schemes of *Archer et al.* [1998] for POM and $CaCO_3$, and *Gnanadesikan* [1999] for opal, with sediment modules employed at 100 m depth intervals. The model was run for a total of 300 ka with inputs to the system of DIC, ALK, and dissolved $SiO_2$ chosen to attain a steady-state consistent with the modern ocean [*Yamanaka and Tajika*, 1996]. It should be noted that since PANDORA considers only seven geographically distinct surface regions, reducing to as few as four at depth, spatial variability in actual ocean biogeochemical conditions is unlikely to be well represented. The exact correspondence between observed and model data must therefore be interpreted with some caution.

Model results are shown in Figure 3-11, demonstrating a number of trends in the ocean. Of particular importance is the clear non-linear increase of opal burial with rain flux (a). There are a number of obvious artefacts present, such as the apparent decrease in mean opal content ($\bar{c}^{opal}$) with increasing rain flux (b), and the decrease in dissolution flux ($fdis^{opal}$) with increasing $\bar{c}^{opal}$ (c). These are likely to be a consequence of unrealistic $CaCO_3$ sediment distributions produced by the overly-simple ocean configuration and biological schemes in PANDORA. Figure 3-12 shows the same model data, but now on an expanded scale and contrasted with observations. The main points that can be drawn from this exercise are;

(1) The model successfully reproduces a number of observed trends, such as in $\bar{c}^{opal}$ as a function of opal rain flux ($fset^{opal}$) as shown in plot (b) and asymptotic silicic acid concentrations in the sediment ($[H_4SiO_4]_{asym}$) as a function of $\bar{c}^{opal}$ (e). The correspondence between model predictions and the relationship deduced from observations relating $[H_4SiO_4]_{asym}$ with $fset^{opal}$ [*Archer et al.*, 2000] is particularly good (d).

(2) The model is much less successful in predicting opal dissolution fluxes across the sediment-water interface ($fdis^{opal}$), which are generally overestimated, as demonstrated in plots (c) and (f).

Overall, considering that the opal diagenesis model was developed from core data taken solely from the Southern Ocean, many aspects of its performance under completely different conditions are in good agreement with observations. That dissolution fluxes at low- and mid-latitude regions tend to be overestimated is much less important in terms of the global mass balance of Si since the Southern Ocean dominates the global sink. However, it will be shown subsequently that the use of a more 'realistic' ocean representation greatly enhances the apparent success of the model (4.5.2).

**Table 3-5** Opal Diagenesis Look-up Table Spanning Set

| Parameter | range | step | units |
|---|---|---|---|
| Sedimentary opal content | 2 to 100 | 2 | % |
| Bottom-water $[H_4SiO_4]$ | 0 to 250 | 10 | $\mu$mol kg$^{-1}$ |
| Bottom-water temperature | 270 to 280 | 1 | K |
| Base dissolution rate, $k_0^{opal}$ | 0.01 to 1.00 | 0.01 | a$^{-1}$ |
| Sedimentary %detrital/%opal | 0 to 10 | 1 | n/a |

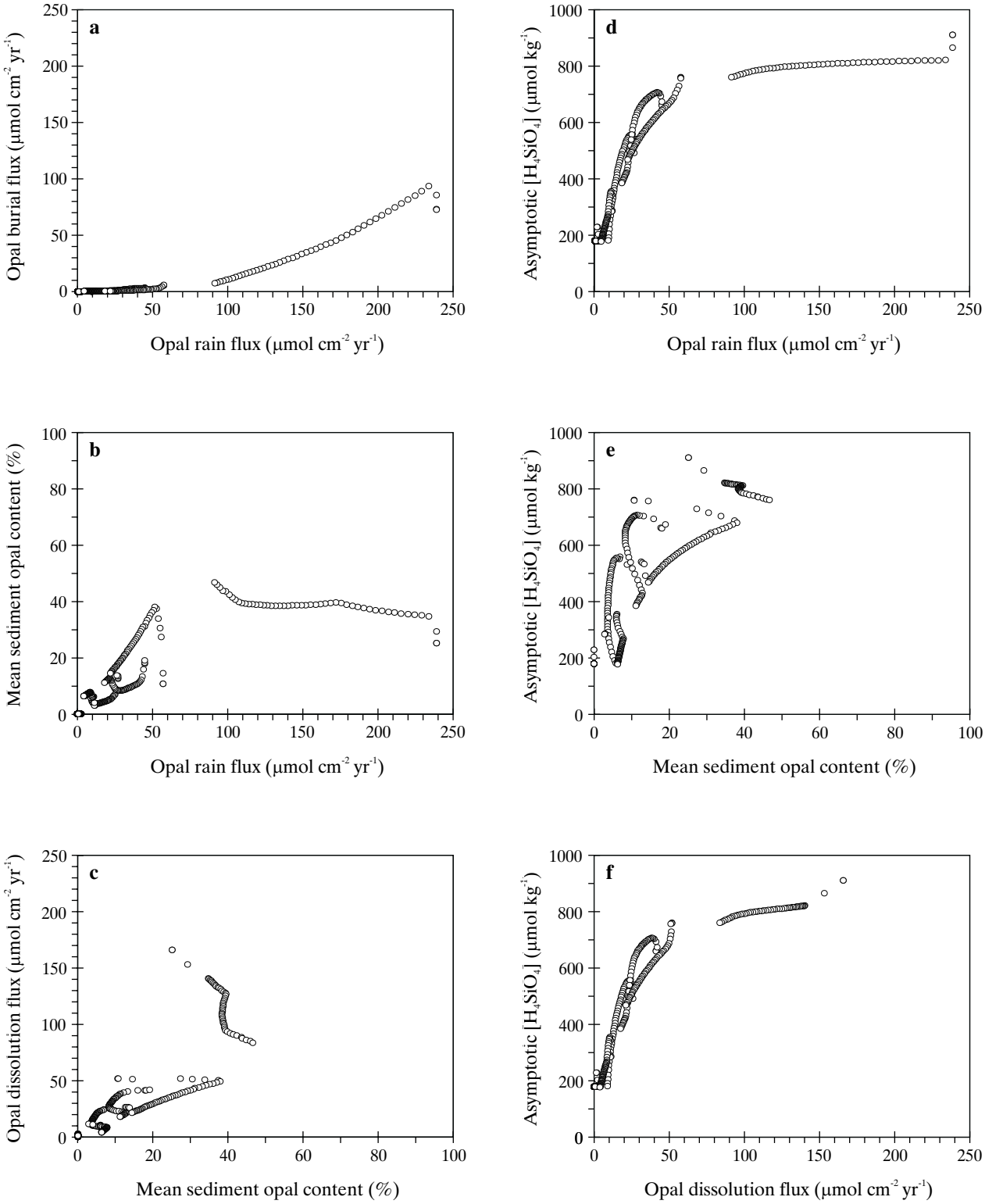


**Figure 3-11** Combined response of the opal diagenesis model within SUE (configured following *Broecker and Peng* [1986]).

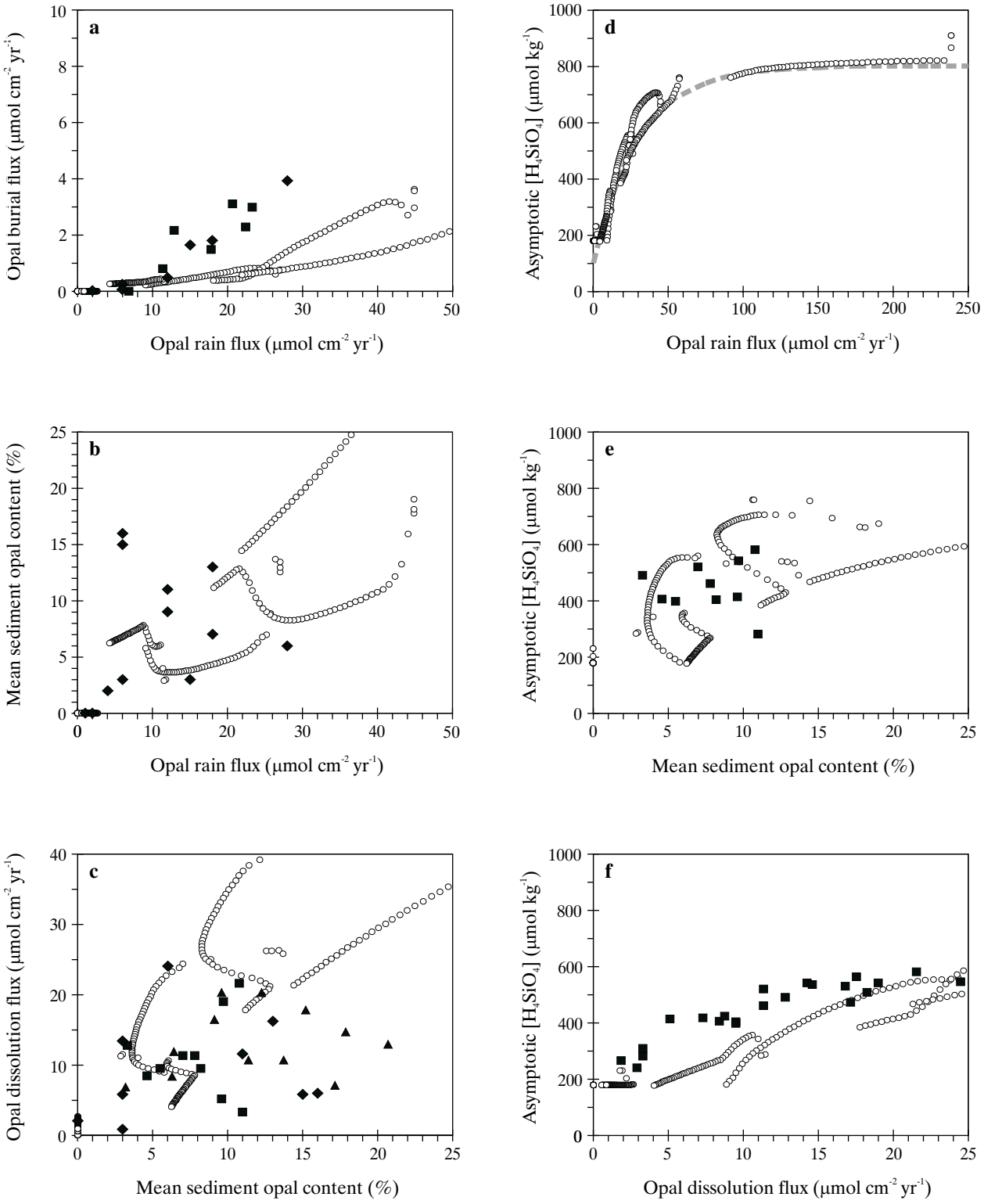


**Figure 3-12** Combined response of the opal diagenesis model within SUE (small open circles) contrasted with the validation data, indicated by larger filled symbols; squares - *McManus et al.* [1995], diamonds - *Archer et al.* [1993], triangles - *Martin et al.* [1991]. The thick dashed grey line in (d) indicates the estimated trend of *Archer et al.* [2000].

## 3.3 Synthetic deep-sea sediment cores

Much of the available information regarding the glacial-interglacial cycles of the late Quaternary comes from sediment cores recovered from the benthic environment. Not only is there excellent global coverage afforded by such records but in addition they contain a large number of proxies relating to different aspects of the state and operation of the Earth system. However, to be of use in understanding glacial-interglacial change these proxies must be interpreted. This is often no easy matter, particularly where a number of separate nonlinear processes all contribute to the observed net change. It may then not be possible to unequivocally deduce the mechanism(s) responsible for this change.

An alternative but very much complementary approach to glacial-interglacial analysis is developed here - working forwards from a description of processes driving the change towards observations. The advantage of this methodology is that the processes operating are explicitly known, and as such can be isolated and fully characterized through sensitivity studies and similar analyses. The possibility of non-unique solutions remains; correctly simulating a paleoceanographic proxy can not prove unequivocally that the model processes involved were actually important. However, use of multiple paleoceanographic proxy indicators can provide powerful additional constraints to a chosen hypothesis.

### 3.3.1 Synthetic sediment core construction

The thickness of accumulating material that the sediment module can track is theoretically limitless. However, in the sediments integral to the model where there is one module associated with every depth interval at each of every ocean grid point, practicalities of data storage forces the maximum number of sub-layers represented to be restricted. Sub-layers at the bottom of the stack are now gradually 'lost' as sediment accumulates at the top of the stack. As long as the depth of sediment represented exceeds the maximum possible thickness that can be lost due to sediment erosion [*Archer et al.*, 1998] the dynamical response of the model will be unaffected.

A second set of sediment modules is introduced, distinct from the 'integral' modules. These are prescribed only at key and/or representative locations in the ocean. This gives a much more manageable number of cores such that enough sub-layers can be represented to enable the entire history of sediment accumulation over the course of the model run to be tracked. Although the representations of sediment deposition, diagenetic alteration, and bioturbation are identical to those acting in the integral modules, these additional core systems are assumed to be completely passive in that there is no exchange of mass with the ocean.

Age scales (i.e., age as a function of depth in the sediment) are provided for these synthetic cores in order to allow direct comparisons to be made with actual cores recovered from the deep sea. A number of different approaches for this are provided for.

*Oxygen isotope stratigraphy*

Age scales for sediment cores recovered from the deep-sea are typically generated by a rather complex procedure involving tuning measured foraminiferal $\delta^{18}O$ stratigraphy to an orbital template [*Berger*, 1994; *Berger et al.*, 1994, 1995, 1996; *Imbrie et al.*, 1984]. The foraminiferal $\delta^{18}O$ colour tracer in SUE provides the raw information to allow this procedure to be followed. However, constructing orbitally-tuned age scales for the huge number of synthetic sediment cores which can be generated from multiple model runs is likely to be very time-consuming. This approach is therefore not adopted for routine use with SUE.

*Single stratigraphic marker*

The simplest approach for down-core age assignment is to assume constant sediment accumulation rates. A single stratigraphic marker is generated by applying an impulse of a conservative colour tracer to the sediment surface at the end of model spin-up (identical to inert tracer profile simulations - 3.2.1.2). The level at which the peak concentration of colour tracer occurs in the core is identified and assumed to have an age equal to that at which the impulse event occurred. Linear interpolation between the age at this depth level and zero at the sediment surface thus defines the sediment age scale. This method is analogous to the use of linear interpolation from the magnetic reversal at the Brunhes-Matuyama boundary to core-top [*Raymo*, 1997], a relatively common technique, particularly in cores lacking a reliable $\delta^{18}O$ stratigraphy [*Farrell and Prell*, 1991]. However, many potential mechanisms for glacial-interglacial change in the global carbon cycle lead to significant variability in sediment accumulation rates. This methodology is thus only of use either with a sub-set of glacial-interglacial hypotheses or for cores located in environments inhibitive to the preservation of calcite (upon which other age scales depend).

*Carbon-14*

Calcitic $^{14}C$ in the sediments is continuously decayed allowing radiocarbon ages to be calculated. However, this is of limited practical use in contrasting extended model and observed core signals. Uncertainties in past cosmogenic production rates, and changes in reservoir capacity [*Stocker and Wright*, 1996], together with analytical considerations all act so as to restrict the age interval over which radiocarbon dating is reliable to within the last full glacial cycle.

*Depositional age tracer*

The advantage of synthetic sediments is that the precise time at which material is deposited to the sediment surface is known. A (calcite-tied) colour tracer representing the time of deposition can be used to provide a mean age for each sediment sub-layer. In light of the various drawbacks associated with the three methodologies outlined above this simple internal age scale is adopted for all further analysis of synthetic sediment cores in the present study.

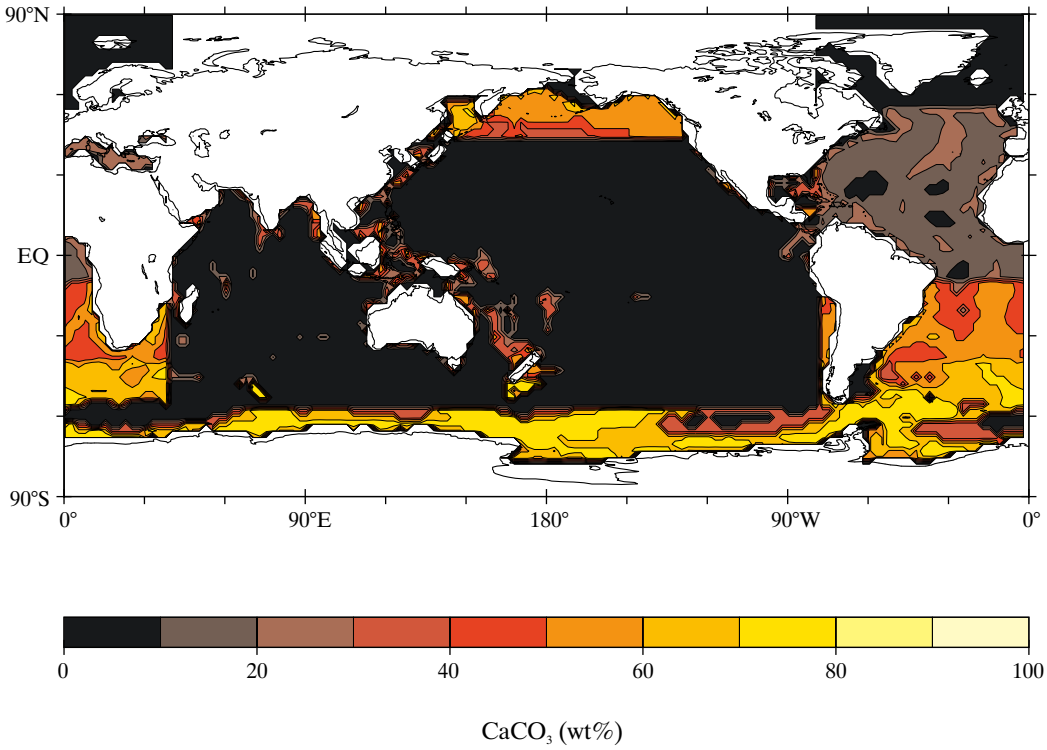


**Figure 3-13** Global distribution of sediment surface $CaCO_3$ generated by SUE (configured after *Broecker and Peng* [1986]), and interpolated to a 2.5° by 2.5° grid.

### 3.3.2 The application of synthetic sediment cores to paleoclimatic analysis

Three primary areas for application of synthetic deep-sea sediment cores to glacial-interglacial paleoclimatic investigation are identified; analysis of the global distribution of sediment composition, general down-core variability within individual cores, and changes in the character of the $CaCO_3$ lysocline transition zone. In the following sections these are exemplified with the aid of the results of a simple carbon cycle model. SUE is run in a 'PANDORA'-type configuration (see 3.2.5.3) for a period of 500 ka following 50 ka of spin-up. The system is perturbed by varying the magnitude of the terrestrial carbon reservoir. The forcing signal for this is a square-wave; period 100 ka, amplitude 1000 GtC, and with a linear transfer of carbon between reservoirs taking place over an interval of 1 ka.

#### *3.3.2.1 Sediment distribution analysis*

Model-generated (core-top) sediment composition and isotopic signatures can be used to produce maps of global distributions. Contrasts with available data sets [*Archer*, 1996b; *Catubig et al.*, 1998; *Henize et al.*, 1999] can give essential diagnostics on the operation of the model carbon cycle and aid in the optimization of unconstrained parameter values. This analysis need not be restricted to the present-day and can be extended back in time, with characteristics extracted from buried sediments for any required period. Comparisons with paleoceanographic observations can then yield important clues as to the past operation of the global carbon cycle. For example, the belt of maximum opal accumulation in the Southern Ocean appears to have migrated northwards at the time of the LGM compared to the present-day [*Anderson et al.*, 1998; *Francois et al.*, 1997; *Kumar et al.*, 1995]; any complete solution for glacial-interglacial change should therefore be able to reproduce such a shift.

Mapping global sediment distributions from results produced by SUE is complicated by the absence of a single ocean floor depth associated with each grid point (as is the case in 3D OGCMs). Instead, each model region has a series of sediment modules which span discrete intervals over the maximum depth of the water column. Distributions are therefore produced for each ocean region in turn by mapping the sediment composition characterizing each sediment module onto all ocean floor lying within the depth interval spanned by that module as defined by observed ocean bathymetry [*ETOPO5*, 1988]. To illustrate this Figure 3-13 shows the global distribution of core-top $CaCO_3$. While the prescribed export fluxes in PANDORA [*Broecker and*

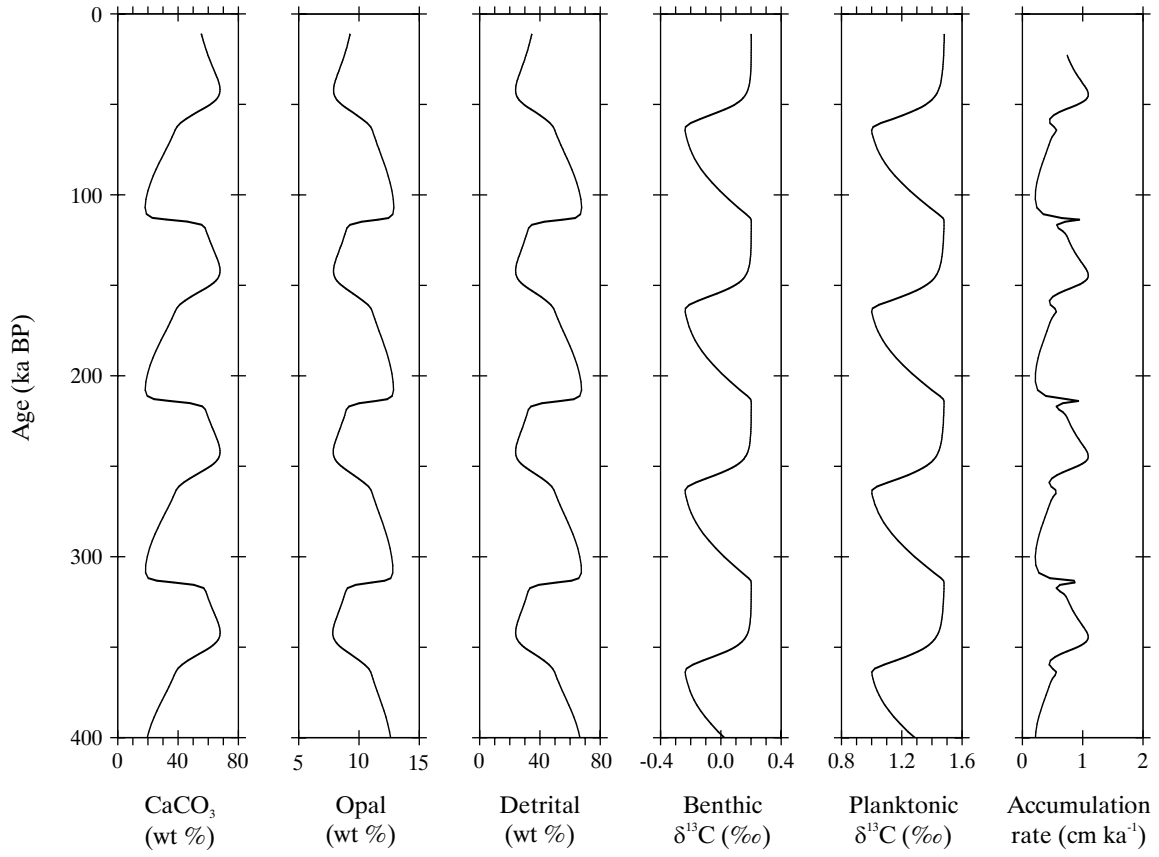


**Figure 3-14** Down-core variability in major sediment solid components, isotopic foraminiferal $^{13}C$ tracers, and overall sediment accumulation rate in a synthetic sediment core located at an intermediate depth in the Southern Ocean. The model is forced by a simple cyclical (square-wave) change in terrestrial carbon storage.

*Peng*, 1986] clearly produce erroneously high $CaCO_3$ preservation in the Southern Ocean with little preservation in the northern Atlantic and Indo-Pacific, this exercise does highlight two important features. Firstly, the depth-dependence of $CaCO_3$ preservation (for instance, the topographic and therefore preservational high of the mid-Atlantic ridge can be picked out). Secondly, distinct regional differences in preservation arising from a combination of the specifics of ocean circulation and biological export can be generated. The boundaries differentiating between the various grid point regions can be seen as sharp linear transitions in $\%CaCO_3$, an artifact of the low spatial ocean resolution of PANDORA.

### *3.3.2.2 Single core analysis*

Of particular interest in this present study of glacial-interglacial change are comparisons that can be made between variability in model and observed down-core sediment characteristics. Ideally, mismatches between model and observations should indicate deficiencies in the model representation of changes in the global carbon cycle. However, in practice such direct analysis is not possible. The information contained in synthetic model sediment cores is determined by processes and environments representing large temporal and spatial means. In contrast, sediment cores recovered from the deep sea may be influenced by local processes such as up-welling [*Bertrand et al.*, 1996] and sediment redistribution by bottom currents [*Bareille et al.*, 1994; *Seidov and Haupt*, 1999]. Moreover, in order to maximize core resolution locations are often deliberately chosen where such local processes result in enhanced sedimentation rates. As a result, the degree of bioturbational filtering in down-core variability is likely to differ substantially between model-generated and observed signals. The respective amplitudes and mean values of such variability cannot therefore be expected to closely correlate. Random events can further increase the specificity of recovered cores, particularly through non-local mixing (such as through burrow formation) and core damage during recovery, but also from turbidity events. These can all result in depth intervals characterized by intense distortion and hiatuses in proxy signals, factors which cannot be prognostically generated by the model.

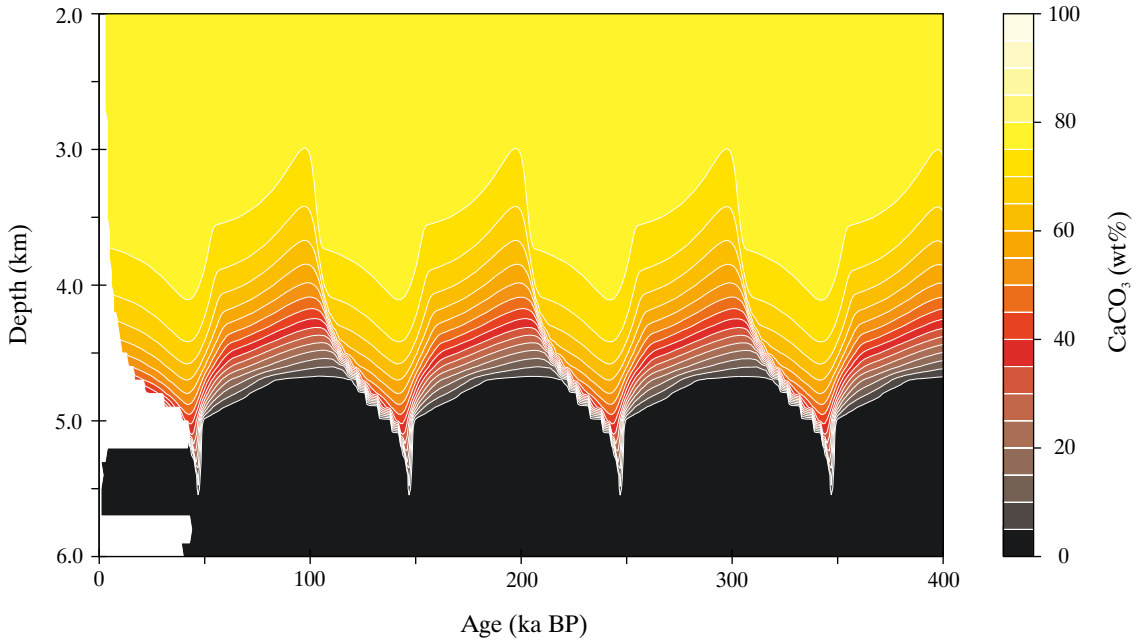


**Figure 3-15** Variability in the shape of the $CaCO_3$ lysocline transition zone with time, as recorded by a series of synthetic sediment cores.

Although processes operating on smaller scales than those represented by the model exert an important control on the observed record there is no reason *a priori* why the timing and direction of change on glacial-interglacial time scales should not generally find a strong correspondence with synthetic proxies (that is where perturbations in the global carbon cycle are correctly represented in the first place). By contrasting the phase of model and observed signals information should be extractable regarding the mechanisms responsible for variability in the system. Visual inspection may often be sufficient for such analysis, although use of spectral methods can naturally provide a more quantitative assessment of the response (e.g., *Hagelberg et al.* [1991]; *Lau and Weng* [1995]; *Mann and Lees* [1996]).

Figure 3-14 shows a sub-set of the paleoceanographic proxy information extractable from a single synthetic sediment core generated by SUE. All are plotted as a function of sediment age for the past 400 ka (equivalent to a total core length of about 229 cm), defined according to the internal calcite-tied age tracer. The effect on the preservation of $CaCO_3$ resulting from changes in ocean chemistry as carbon is alternately removed from and added to the ocean can be clearly seen, with the relative proportions of the other major solid phase responding in anti-phase. In this particular model run $^{13}C$ fractionation in benthic and planktonic foraminifera is assumed to follow that for bulk calcite (2-61a), such that variability in $\delta^{13}C^{foram}$ reflects only changes in the mean isotopic composition of the ocean as a whole. Finally, pronounced changes in sediment accumulation rate are apparent. Use of an age scale derived from a single stratigraphic marker with the assumption of constant accumulation rate (3.3.1) would obviously therefore produce a distorted picture were it to have been adopted in this example.

### *3.3.2.3* $CaCO_3$ *lysocline transition zone*

Although there is no precise definition, the location of the calcium carbonate (as either calcite or aragonite) lysocline is often taken to mark the depth in the ocean at which the presence of $CaCO_3$ starts to decline rapidly in surface sediments with increasing depth [*Berger*, 1968; *Balsam*, 1983; *Broecker and Takahashi*, 1978; *Farrell and Prell*, 1989]. A second characteristic feature of deep-sea sediment composition is the carbonate compensation depth. This is the point at which the $CaCO_3$ dissolution flux is exactly balanced by the rain rate and is usually taken to be the depth where $CaCO_3$ first disappears from the sediments [*Farrell and Prell*, 1989]. Between these lies the lysocline transition zone.

In any restricted region of the ocean, the depth and thickness of the lysocline transition zone will vary on glacial-interglacial time scales as a result of changes in ocean chemistry and/or particulate rain rates to the sediment surface. Analysis of past changes in this zone obtained by comparison of model simulation with observations can thus provide important information regarding the operation of the carbon cycle. Although a number of studies report past variability in the depth profiles of both calcite and aragonite sediment content [*Balsam*, 1983; *Berger*, 1977; *Farrell and Prell*, 1989, 1991; *Karlin et al.*, 1992] there has only been one modelling attempt to date [*Walker and Opdyke*, 1995].

To reconstruct glacial-interglacial variability in the depth and shape of the calcite and aragonite lysocline transition

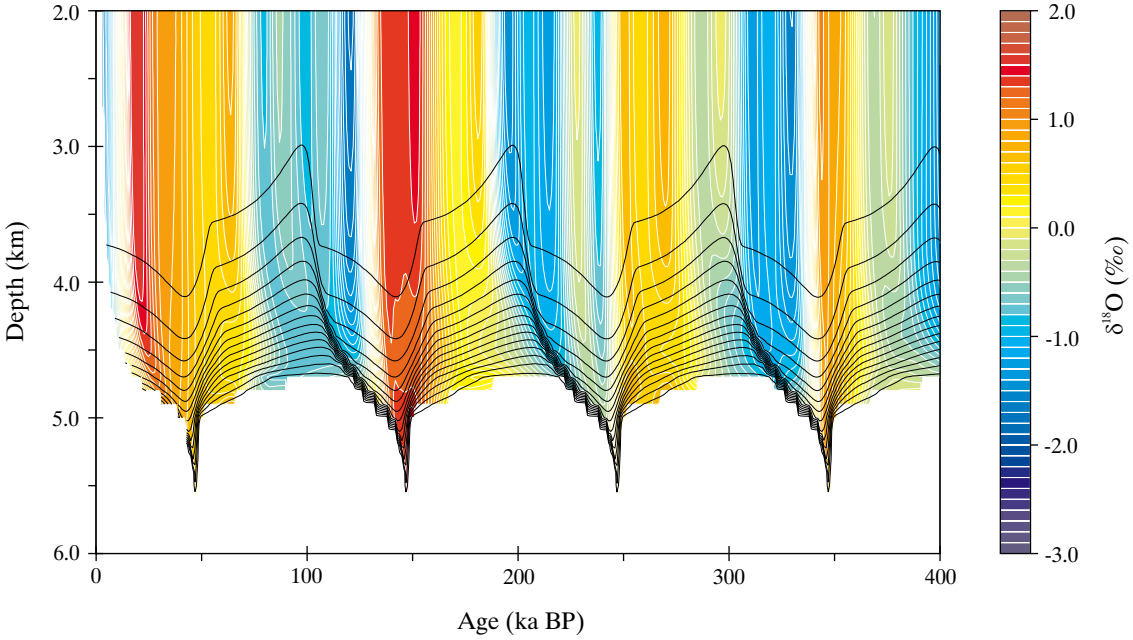


**Figure 3-16** Variability in the synthetic foraminiferal $\delta^{18}O$ tracer over the $CaCO_3$ lysocline transition zone with time, together with contours of $CaCO_3$ content (see Figure 3-15).

zones a series of synthetic sediment cores are defined within the same grid point region and at closely spaced depths. Figure 3-15 shows how the shape of the $CaCO_3$ lysocline transition zone changes over the past 400 ka in response to the applied terrestrial carbon storage forcing. It can be seen that there is a pronounced cyclicity in both lysocline and carbonate compensation depths over this period, with a peak-to-peak amplitude of about 1 km. Pronounced preservation spikes during times of rapid carbon transfer out of the ocean-atmosphere system are also present.

Other sedimentary characteristics can be plotted in a similar manner. Figure 3-16 shows the distribution of the synthetic foraminiferal $\delta^{18}O$ tracer over the same depth and time range as before. In the absence of any explicit representation of $^{18}O$ fractionation within the system (2.2.1.2), sediment boundary conditions are provided by simply assuming an isotopic signature of settling $CaCO_3$ reaching the sediment surface equal to the equivalent value dictated by the SPECMAP $\delta^{18}O$ signal [*Imbrie et al.*, 1984] at the time of deposition. It should be noted that while use of SPECMAP gives a first-order representation of observed glacial-interglacial variability in $\delta^{18}O$, the mean and amplitude of this stacked record are somewhat artificial in value. That maxima and minima in $\delta^{18}O$ occur approximately simultaneously at all depths down through the water column suggests that even during episodes of intense erosion or preservation, the internal model age scale should be comparable to one derived via orbital tuning of the down-core $\delta^{18}O$ signal.